

Correlation of multi-temporal ground-based optical images for landslide monitoring

Julien Travelletti, Christophe Delacourt, Pascal Allemand, Jean-Philippe Malet, Jean Schmittbuhl, Renaud Toussaint, M. Bastard

▶ **To cite this version:**

Julien Travelletti, Christophe Delacourt, Pascal Allemand, Jean-Philippe Malet, Jean Schmittbuhl, et al.. Correlation of multi-temporal ground-based optical images for landslide monitoring. ISPRS Journal of Photogrammetry and Remote Sensing, 2012, 70, pp.39-55. 10.1016/j.isprsjprs.2012.03.007 . insu-00694179

HAL Id: insu-00694179

https://insu.hal.science/insu-00694179

Submitted on 15 May 2019

HAL is a multi-disciplinary open access archive for the deposit and dissemination of scientific research documents, whether they are published or not. The documents may come from teaching and research institutions in France or abroad, or from public or private research centers.

L'archive ouverte pluridisciplinaire **HAL**, est destinée au dépôt et à la diffusion de documents scientifiques de niveau recherche, publiés ou non, émanant des établissements d'enseignement et de recherche français ou étrangers, des laboratoires publics ou privés.

Elsevier Editorial System(tm) for ISPRS Journal of Photogrammetry and Remote Sensing

Manuscript Draft

Manuscript Number:

Title: Correlation of multi-temporal ground-based images for landslide monitoring: application, potential and limitations.

Article Type: Full Article

Keywords: image cross-correlation; image matching; landslide; time-lapse photography; displacement monitoring

Corresponding Author: Dr. Jean-Philippe Malet,

Corresponding Author's Institution: CNRS / IPGS

First Author: Julien Travelletti

Order of Authors: Julien Travelletti; Christophe Delacourt; Pascal Allemand; Jean-Philippe Malet; Jean Schmittbuhl; Renaud Toussaint; Mickael Bastard

*Manuscript
Click here to download Manuscript: IJPRS-Travelletti_et al_SUBMITTED-VERSION_manuscript.pdf Click here to view linked References

Correlation of multi-temporal ground-based images for landslide monitoring: application, potential and limitations.

Travelletti J. (1,2), Delacourt C. (3), Allemand P. (4), Malet J.-P. (1), Schmittbuhl J. (1), Toussaint R. (1), Bastard M. (1)

(1) Institut de Physique du Globe de Strasbourg, CNRS UMR 7516, Université de Strasbourg / EOST, 5 rue René Descartes, 67084 Strasbourg Cedex, France. E-mail: julien.travelletti@unistra.fr
(2) GEOPHEN - LETG, CNRS UMR 6554, Université de Caen Basse-Normandie, Caen, France
(3) Institut Universitaire Européen de la Mer, CNRS UMR 6538, Université Européenne de Bretagne, Brest, France.
(4) Laboratoire des Sciences de la Terre, CNRS UMR 5570, Université de Lyon & Ecole Normale Supérieure, Lyon, France.

Abstract

The objective of this work is to present a low-cost methodology to monitor the displacement of continuously active landslides from ground-based optical images analyzed with a normalized Image Correlation technique. The performance of the method is evaluated on a series of images acquired on the Super-Sauze landslide (South French Alps) over the period 2008-2009. The image monitoring system consists in a high resolution optical camera installed on a concrete pillar located on a stable crest in front of the landslide and controlled by a datalogger. The data are processed with a cross-correlation algorithm applied on the full resolution images in the acquisition geometry. Then, the calculated 2D displacement field is ortho-rectified with a back projection technique using a high resolution DEM interpolated from Airborne Laser Scanning (ALS) data. The heterogeneous displacement field of the landslide is thus characterized in time and space. The performance of the technique is assessed using as reference differential GPS surveys of a series of benchmarks. The sources of error affecting the results are then discussed. The strongest limitations for the application of the technique are related to the meteorological, illumination and ground surface conditions inducing partial or complete loss of coherence among the images. Small changes in the camera orientation and the use of a mono-temporal DEM are the most important factors affecting the accuracy of the ortho-rectification of the displacement field.

Because the proposed methodology can be routinely and automatically applied, it offers promising perspectives for operational applications like, for instance, in early warning systems.

Keywords: image cross-correlation; image matching; landslide; time-lapse photography; displacement monitoring

1 Introduction

Displacement monitoring of unstable slopes is a crucial tool for the prevention of hazards. It is often the only solution for the survey and the early-warning of large landslides that cannot be stabilized or that may accelerate suddenly and potentially fluidize in highly mobile mudflows. The choice of an adequate monitoring system depends on the type and size of landslide, the range of observed velocity, the required frequency of acquisition, the desired accuracy and the financial constraints. Displacement monitoring techniques applied on landslides can be broadly subdivided in two main groups: geodetic and remote-sensing techniques.

Geodetic surveying consist in detecting geometrical changes in the landslide topography by measuring geometric parameters such as angles, distances or differences in elevation (e.g. levelling, tacheometry; Meissl & Naterop, 1995). These techniques necessitate the installation of benchmarks or targets in and outside the landslide and in measuring their position at different times. They have the advantage to be very accurate (0.2 to 2.0 cm) with a high potential of automation (Malet et al., 2002; Jaboyedoff et al., 2004; Foppe et al., 2006). Furthermore, many authors demonstrated the efficiency of permanent (Malet et al., 2002) and non-permanent (Squarzoni et al., 2005; Brunner et al., 2007) differential Global Positioning System (dGPS) for landslide monitoring with a centimetric accuracy during any daytime and weather conditions. However, because landslides can show highly variable displacement rates in time and space according to the local slope conditions (bedrock geometry, distribution of pore water pressures), the major drawbacks of the geodetic techniques are (1) to provide only discrete point measurements of the displacement and (2) the costs of installation and maintenance of the survey network. They are usually only justified in the case of a real risk for the population.

Remote-sensing techniques appear to be an interesting and complementary tool to obtain spatially-distributed information on the kinematics (Delacourt et al., 2007) which is also justified by the need to investigate landslides from safe and remote places because of the inaccessibility of mountainous terrains. Remote-sensing techniques give the possibility to discriminate stable and unstable areas and to map sectors within the landslide with different kinematics from a regional to

66 a local scale. They are also useful tools for a process-based analysis of the deformation field
67 affecting the slope (Casson et al., 2005; Teza et al., 2008; Oppikofer et al., 2008). Remote-
68 sensing techniques can be operational from spaceborne, airborne and ground-based platforms. In
69 the last decades, the development of ground-based platforms for landslide monitoring at the local
70 scale provided many advantages over spaceborne and airborne platforms despite a shorter spatial
71 coverage (Corsini et al., 2006). The geometry and frequency of acquisitions are more flexible and
72 adaptable to any type of local environment. Furthermore, the installation of the monitoring system
73 is generally relatively easy. In addition ground-based platforms are permanent installations that
74 allow a continuous monitoring (Casagli et al., 2004; Delacourt et al., 2007). Three main
75 categories of ground-based remote sensing techniques are used in landslide monitoring: Ground-
76 Based Synthetic Aperture Radar Interferometry (GB-InSAR), Terrestrial Laser Scanning (TLS)
77 and Terrestrial Optical Photogrammetry (TOP). A non exhaustive review of the main advantages
78 and disadvantages of these techniques is presented in Table 1. Detailed reviews of the application
79 of GB-InSAR and TLS to landslides can be found in Luzi (2010), Corsini et al. (2006),
80 Tarchi et al. (2003), Jaboyedoff et al. (2010), Teza et al. (2007, 2008) and Monserrat & Crosetto
81 (2008). A state-of-the art of the application of TOP to landslide and related geomorphologicla
82 processes is given below.
83 TOP is a very cost-effective technique with implementation, operating and equipment costs much
84 lower than GB-InSAR and TLS. The technique consists in acquiring digital optical images
85 represented using a matrix of intensity values (brightness) recorded at each pixel of the Charge
86 Coupled Device (CCD) of the camera. While aerial images are acquired on overhead photographs
87 from an aircraft, TOP uses RGB images acquired from a spot very close to the ground (Jiang et
88 al., 2008). In the last decades, camera self-calibration and analytical processing techniques allow
89 the use of non-metric cameras and of simplified camera calibration algorithms to compute digital
90 elevation models using the principle of stereoscopic views (Mikhail et al., 2001; Jiang et al.,
91 2008). In the current state, the application of terrestrial images for landslide monitoring is mostly
92 related to the production of DEMs for image ortho-rectification and sediment budget analysis
93 (Bitelli et al., 2004, Pesci et al., 2004; Cardenal et al., 2008), and more recently to the
94 characterization of the slope morpho-structure (Lim et al., 2005; Sturzenegger & Stead, 2009).
95 Using correlation techniques, two-dimensional displacement fields can be derived by tracking
96 objects in two images acquired at different time. So far, image correlation techniques have been
97 applied only on aerial and satellite images (e.g. SPOT, QuickBird, OrbView, EROS) for the
98 creation of landslide displacement maps (Casson et al., 2003; Delacourt et al., 2004; LePrince et
99 al., 2008); the use of image correlation on terrestrial images has not been as popular for

permanent landslide monitoring as in other application field such as in solid and fluid mechanics for the characterization of the deformation pattern of soil/rock samples (White et al., 2003; Chambon et al., 2003; Küntz et al., 2005) or for the monitoring of other natural processes such as ice glaciers (Corripio et al., 2004; Fallourd et al., 2010; Maas et al., 2008) or volcanoes (Honda & Nagai, 2002). Only Delacourt et al. (2007) demonstrated an efficient application of TOP for landslide monitoring which consisted in the determination of the landslide boundaries and in the qualitative estimation of the spatial variability of displacement at the La Clapière landslide (French Alps) with an image acquisition system installed at 1 km-distance.

Generally, the 2D displacements (in pixel) evaluated by the correlation algorithm have an accuracy of about 0.2 pixel (Casson et al., 2005; Delacourt et al., 2007) in the image plane, corresponding to an accuracy of millimeters to several centimeters for distances of about 100 m in the local coordinate system (Kraus & Waldhäusl, 1994).

The major sources of errors affecting the displacement calculations and thus potentially limiting the efficiency of TOP for an operational landslide monitoring can be classified in two groups: (i) the parameters affecting the Image Correlation computation and (ii) the external parameters influencing the ortho-rectification procedure.

The objective of this work is therefore to evaluate the potential and the limitations of TOP for the permanent monitoring of landslide using Image Correlation (IC) techniques. The dataset of images available for the Super-Sauze landslide (South French Alps) for the period 2008-2009 is used. First, the steps in the data acquisition and data processing (image correlation, ortho-rectification) are presented and the results are evaluated using the displacement of benchmark measured by DGPS. Second, the main advantages and disadvantages of the method, and the influence of external factors on the precision and the accuracy of the results are discussed. Throughout this work, the accuracy is defined as the systematic difference between a measured quantity and the true value, and precision is defined as the random difference between multiple measurements of the same quantity.

2 Experimental Site: the Super-Sauze landslide

To evaluate the potential of correlation of ground-based images for landslide monitoring, the dataset available at the Super-Sauze landslide, triggered in the Callovo-Oxfordian black marls of the South French Alps (Alpes-de-Haute-Provence, France; Fig. 1A, 2A, B) is used. The landslide is located in the upper part of the Sauze torrential catchment. In the 1960s, the area was affected by rock failures in the scarp area. The failed material composed of rocky panels progressively

transformed into a silty-sandy matrix integrating marly fragments of heterogeneous sizes through successive weathering cycles (Malet et al., 2003). From the 1970s until today, the landslide material is gradually filling a torrential stream located downstream with a typical range of displacement rate between 1 to 3 $cm.d^{-1}$ on average and possible higher velocities up to 40 $cm.d^{-1}$ during acceleration periods (Malet et al., 2002). In 2007, the mudslide extent over a distance of 920 m between an elevation of 1980 m at the scarp and 1760 m at the toe with an average width of 135 m and a average slope of 25°. The total volume is estimated at 560,000 m^3 (Travelletti & Malet, submitted).

The kinematics of the landslide is currently monitored by Differential Global Positioning System (DGPS) and Terrestrial Laser Scanning (TLS), and by a remote camera monitoring system. This instrumentation consists in a low-cost D70 Nikon non-metric reflex digital camera installed on a concrete pillar located on a stable crest in front of the landslide at a distance of 300 m from the lower part and 900 m from the main scarp (Fig. 1A, B, C). The acquisition system is controlled by a datalogger (Campbell CR10) and the power is provided by a 40 W solar panel. The characteristics of the acquisition are presented in Table 2. Each four days, four images are acquired at 11:00, 12:00, 13:00 and 14:00 GMT in order to increase the probability of having at least one image with good meteorological conditions. Each photograph (6 Mb) is stored in a native file format to avoid any loss of information.

3 Methodology

The steps in the data processing workflow consist in (1) correlating the images by pairs in their original acquisition geometry to prevent any loss of information, and (2) ortho-rectifying the calculated displacement fields using a high-resolution digital elevation model interpolated from airborne LiDAR data. The daily images presenting the best ground texture contrast and the most homogeneous lightening are selected based on expert judgment. The detailed methodology is summarized in Fig. 3 and described below.

3.1 Principle of the Image Correlation technique

The 2D displacement field is obtained by correlating two optical images acquired at different time. The image correlation technique is based on the automatic identification of identical texture patterns within an image by maximizing a correlation function (Lewis, 1995; Baratoux et al., 2001; Debella-Gilo & Kääb, 2010). Its principle adapted for landslide kinematics analysis is described in Delacourt et al. (2007). Visible ground features have to be superimposed on two

successive images on stable parts located outside the landslide. On the areas affected by landslide movements, the visible and recognizable features are shifted by the displacements. In order to quantify the ground displacements, a correlation window is defined on a reference (often the oldest) image. The corresponding window is searched in a pre-defined explored area belonging to the second image. The starting point of this explored area is the expected position of the window as if no displacement occurred between two acquisitions. The process is repeated for each pixel of the reference image. The Euclidean distance between the reference point and the matching point represents the displacement magnitudes in the image plane. By modifying the zone of interest, it is then possible to determine the displacements at various positions within the images (Fig. 4). It is important to note that the normalized cross-correlation technique cannot track objects that start to rotate significantly or are affected by important perspective distortions (Lewis, 1995).

The size of the correlation window is a compromise between the desired accuracy on the displacement estimates and the spatial resolution of the velocity field (Delacourt et al., 2007). An increase of the size of the correlation window ensures a good signal to noise ratio and thus a good precision, but the accuracy on the displacement estimates decreases because of their averaging on a larger correlation window. This compromise is difficult to find when some parts of the landslide are well defined in terms of ground texture while others parts are not. Hierarchical correlation techniques allow to overcome this problem by automatically changing the physical size of the correlation window and of the explored area during the correlation computations. The physical size is defined as the effective landslide surface covered by the correlation window (Rohaly, 2002; Aloui & Ibn-Elhaj, 2009).

In this work, a sub-pixel hierarchical correlation technique is used (Chambon, 2003; Bastard, 2009). The RGB images are first converted in gray-scale images on which a 3x3 pixel Sobel convolution matrix is applied to highlight the ground surface texture. The gradient values are then correlated (Chambon, 2003). Four successive degradations of the image resolution are applied following a pyramidal approach for changing the physical size of the correlation window and of the explored area by down-sampling the gradient values of the full resolution image (D'Antone, 1995; Kumar & Banerjee, 1998) (Fig. 4). The optimum sizes of the correlation window (16x16 pixels) and of the explored area (32x32 pixels) were identified with a trial and error procedure. These parameters are constant during the correlation computation. The correlation starts with the lowest resolution image in order to determine the largest displacements. Then the location of the pixel with the maximum cross-correlation value is used as the centre of the zone of interest for the next correlation step at a higher resolution. The spatial location of the maximum correlation value in the highest resolution image is thus progressively better estimated (Fig. 4). Ignoring high

resolution information at the first computational step decreases the probability to reach a local minima of the correlation function and, consequently, to obtain wrong matches in the correspondence solutions (Aloui & Ibn-Elhaj, 2009). In addition, this approach ensures a higher probability of reliable correlation peak detection (Anandan et al., 1993). The sub-pixel displacement is computed after the correlation at the highest resolution image. An iterative procedure is used to find the maxima of the correlation function interpolated with a bi-parabolic formula and with a maximization procedure based on the simplex method (Press et al., 1997; Chambon, 2003).

The correlation results consist in matrices of displacements Δu and Δv along the u- and v-axes in the image plane with their associated correlation index (Fig. 4). Because the pixel size is not constant in the image due to the oblique acquisition, the displacements field correlated in the image plane cannot be directly interpreted in terms of metric displacements. Therefore an ortho-rectification procedure is necessary for a quantitative analysis of the displacement fields.

3.2 Ortho-rectification of the displacement field using high-resolution digital elevation models (DEMs)

The ortho-rectification procedure consists in transforming the central projection of the image into an orthogonal view of the ground by correcting the effects of various distortion sources such as camera orientation, topographic effects and lens characteristics (Kraus & Waldhaüsel, 1998). In terrestrial photogrammetry, distortions induced by topography effects are the most important due to the oblique acquisition of the images. The ortho-rectification is used to convert the initial (u,v) and the final $(u+\Delta u,\ v+\Delta v)$ positions of the displacement vectors in a local coordinate system. The conversion is possible if a Digital Elevation Model (DEM) of the object is available in order to relate two-dimensional pixel positions in the image plane to three-dimensional points in a local coordinate system using parametric approaches (Hemmleb & Wiedemann, 1997).

In our approach, the rotation angles defining the external orientation of the camera are first determined using the relationship between the image coordinates (u,v) and the local coordinates system (X,Y,Z) given by the collinearity equations. These equations are based on the principle that each point in the local coordinate system is projected with a straight line through the projection center (origin of the camera) into the image plane (Bonneval 1972, Kraus & Waldhaüsel, 1994). Knowing the exact location of the camera and assuming that the principal point coordinates is at the center of the image, the external angle defining the absolute orientation of the camera in the local reference system can be determined with Ground Control Points (GCPs; Corripio, 2004).

231 In our case, the GCPs located on the landslide by DGPS measurements consisted in red-yellow
232 squared metal targets with a dimension of 0.5x0.5 m identified both in the image plane and in the
233 local coordinate system. A serie of 95 pairs of GCPs distributed on the image plane and in the
234 local reference system were measured (Fig. 5). The centers of the GCPs are positioned in the
235 local coordinate system with an average 3D accuracy of 0.02 m and a standard deviation of
236 0.01 m. The coordinates (u,v) of the GCPs in the image plane are determined by manual picking
237 with an estimated accuracy of about 2 pixels. Among the 95 GCPs, 45 are used to compute the
238 external parameters and 40 are kept to calculate the accuracy of the transformation (section §
239 5.2.1). A least mean square minimization technique based on Singular Value Decomposition
240 (SVD) between observed and calculated GCPs in the image plane is used to determine the
241 external parameters that satisfy the collinearity equations (Heikkilä & Silven, 1997).
242 Then, a backward projection method is applied to allocate a 3D coordinate to each pixel
243 coordinate in the image plane (Mikhail et al., 2001; Corripio, 2004). In the backward projection,
244 instead of interpolating in the local reference system, the interpolation is carried out in the image
245 geometry. A bilinear interpolation is used to associate the X,Y,Z coordinates for each initial point
246 (u,v) and each final point ($u+\Delta u,\ v+\Delta v$) in the image plane. Because the interpolation of the X,Y,Z
247 coordinates is carried out directly on a regular grid, this method is easier to implement than the
248 classical forward method which projects the image location in the DEM geometry (Mikhail et al.,
249 2001). Moreover, a forward projection would transform the pixel coordinates in the image plane
250 to irregularly distributed points in the local reference system which are then interpolated into a
251 regular grid. Therefore, each point of the DEM is projected in the image using the collinearity
252 equations. Because stereoscopic pairs of images acquired simultaneously from two cameras at
253 different view spots are not available because of the local site configuration, two Airborne Laser
254 Scanning (ALS) dense point clouds acquired in October 2007 and July 2009 have been used to
255 interpolate 0.25m mesh-size DEMs with a planar and elevation accuracy of 0.07 m. The
256 displacement correlated during the year 2008 and 2009 were orthorectified using the DEMs of
257 2007 and 2009 respectively In order to avoid the projection of duplicate points in the same
258 position, the points of the DEMs visible from the camera viewpoint are identified by using the
259 sightline method (Fisher, 1994; Franklin & Ray, 1994). The sightline is defined as the straight
260 line going from the camera location to the position located in the gridded DEM. The visible
261 points of the DEM of 2009 are presented in Fig 2B. About 57 % of the landslide area is visible
262 from the camera view point, no displacements can be obviously measured in the invisible areas.
263 The visible points of the DEM are then back-projected and linearly interpolated in the image
264 plane. Three grids for the X, Y and Z coordinates (Fig. 3) are then obtained. The re-projection of

the displacement vector components in the local reference system is then straightforward, and the re-projected vector components are averaged and smoothed in a regular grid with a mesh size of 1m.

The use of a mono-temporal DEM for the ortho-rectification of the displacements is a strong hypothesis that the global landslide morphology remains constant over the period and affect the accuracy of the conversion of the displacement vector in the local coordinate system. However, it will be further demonstrated that this method is still a relevant estimation for our purpose with reference to the amplitude of the observed displacements.

3.3 Image resolution at the terrain surface

The effective (e.g. ground) pixel size is calculated with the DEM of 2009 projected in the image geometry. The effective pixel size is one limiting parameter for the accuracy of the correlation. The pixel size depends on (1) the distance between the object and the camera (Fig. 6A) and (2) the angle of incidence which is defined as the complementary angle between the line of sight of the camera and the normal of the terrain surface (Fig. 6B). A low incidence angle means that the line of sight is nearly tangential to the topography. Consequently, the pixel projection in the local coordinate system is very close to an invisible zone from the camera view point.

The pixel size determines the minimum theoretical displacement that can be detected by the Image Correlation technique for a pixel-level correlation. Below this displacement threshold, the accuracy solely depends on accuracy of the sub-pixel correlation. Globally, the incidence angle on the landslide ranges from 0° to 40° and the pixel size varies from 1.10^{-2} m^2 in the lower part (at an average distance of 300m) to 3.10^{-2} m^2 in the upper part of the landslide (at an average distance of 900 m; Fig. 6A,B). The upper part is characterized with a pixel size often larger than 0.04 m^2, especially in areas where the angle of incidence is less than 5°. Therefore the lowest accuracy is expected in this region because a small Δv and Δu displacement can lead to an important ΔX, ΔY, ΔZ metric displacement.

In order to better assess the effect of the image resolution on the displacement estimate, a rigid displacement of Δv=1 pixel and Δu=1 pixel is imposed for each (u,v) location in the image plane and then converted in the local reference system. The metric displacements plotted versus their corresponding angle of incidence and the histograms with the cumulative distribution function of the displacements are presented in Fig. 7. If only a pixel-level correlation technique is used, the calculated displacements correspond to the minimum displacements that can be detected along the u-axis and v-axis of the image. In areas where the incidence angle is less than 5°, the minimum displacement drastically increases to several meters for both directions (Fig. 7A, B).

Therefore no strong confidence is given to areas whose incidence angle is lower than 5°. 11% and 2% of the pixels in the landslide area with an angle of incidence lower than 5° has a metric sensitivity to one pixel of displacement greater than 0.5 m in the *v*-axis and the *u*-axis (Fig. 7C, D). Globally, 50% of the pixels in the image plane inside the landslide area show a metric sensitivity less than 0.17 m for one pixel displacement along the *v*-axis and 0.07 m along the *u*-axis. Minimum displacements for a pixel-level correlation in respectively the *u* and *v*-direction are 0.04 m and 0.06 m in the lower part of the landslide and 0.09 m and 0.11 m in the upper part.

3.4 Post-processing: displacements filtering

Filtering criteria are necessary to remove the badly correlated points and improve the signal to noise ratio (Casson et al., 2003; Berthier et al., 2005; Wangensteen et al., 2006; Debella & Kääb, 2010). Three criteria are used in this study to filter aberrant displacements in the image plane coordinate system and in the local coordinate system. There are based on:

1. the value of the correlation peak coefficient: loss of coherence can occur during the correlation computations because change in surface states between a reference image and the correlated image are high, resulting thus in low correlation coefficients. Defining a threshold value has the consequence to increase the percentage of realistic displacements. A high threshold coefficient of r=0.6 was selected to remove the badly correlated points. However, the correlation peak coefficient alone is not a sufficient discriminating criteria because some points can display a high correlation coefficient even if they do not represent the same object (e.g. two trees or large stones having the same geometry; Casson et al., 2005);
2. the value of displacement amplitudes and directions: points which detect an upslope displacement detection and a too important displacement amplitude with reference to prior knowledge on the landslide kinematics.
3. the displacements assigned to invisible areas from the camera viewpoint because of small ortho-rectification errors in the conversion to the local coordinate system.

Table 2 presents the results of the filtering on the total number of correlated points. Displacements correlated from images acquired in the summer season (23–27 July 2008) and in the autumn season (19–23 October 2008) highlight the differences in the number of remaining values for the two seasons. The amount of remaining point after filtering varies between 80% and 90% in the summer period and can decrease to 50% in the autumn period. This is mainly explained by the different illumination conditions (low sun elevation) that affect the quality of the correlation. This aspect will be discussed further in section §6.1.3. The upper part of the landslide

331 is the most affected by the filtering criteria. This part generally shows a percentage of remaining
332 values lower than in the middle and lower parts of the landslide. This is explained by the fact that
333 the upper part has a more complex morphology. Consequently the effects of illumination changes
334 are more important than in the middle and the lower parts, especially in autumn. In addition, the
335 angle of incidence in this area can be low (5 to 10°) and thus sensitive to small displacements of
336 the camera.

337 4 Results

338 4.1 Displacement maps of the landslide

339 A set of images over the period May–July 2008 is used to illustrate the potential of the technique
340 for the characterization of the kinematics during an acceleration period triggered by high rainfall
341 amounts and a fast melting of the snow cover.
342 Figure 8 shows an example of displacement rate (in pixel.day^{-1}) of the ground surface in the
343 image plane derived from image pairs of 20–28 May, 1–4 June and 9 June–13 June. The reference
344 is the image of 20 May. The contrast in displacement rates between the landslide area and the
345 stable area gives confidence on the calculated velocity field. One can notice that the pattern of
346 displacement rate is heterogeneous spatially and temporarily. The upper part of the landslide
347 displays the highest velocities ranging from 1 to 7 pixels.day^{-1} while the lower part displays
348 velocities of less than 4 pixels.day^{-1}. No quantitative comparisons can be carried out at this stage
349 because the pixel sizes vary strongly in the image (Fig. 6A). From the 20 May to the 13 June,
350 cumulated displacements up to 110 pixels are observed in the upper part. The maximum of
351 displacement rate is observed around the 1st June. Then the landslide decelerates to displacement
352 rate of about 1 pixel.day^{-1}.
353 Some local specific displacement patterns are also clearly highlighted; for instance, the presence
354 of a stable *in-situ* crest located in the landslide body is perfectly identified in the correlated
355 images.
356 Figure 9 presents the amplitude of the 3D ortho-rectified displacement rates for the period 1st
357 June– 4th June in the local coordinate system. The difference of kinematics among the upper (until
358 3 m.day^{-1}) and the lower (until 1 m.day^{-1}) parts becomes more evident than in the image plane.
359 The geometrical effect induced by the presence of the stable *in-situ* crest on the landslide
360 kinematics is also clearly pointed out. The temporal evolution of the displacement rates is
361 illustrated with two transversal and one longitudinal profiles on Figures 9 and 10. The difference

of displacement rates between the upper and the lower part of the landslide is particularly pointed out.

The precision of the computed displacements is assessed by performing a null hypothesis on the stable areas (Berthier et al., 2005; Casson et al.,2003). Only the points with a correlation coefficient r> 0.8 are taken into account. In the image plane coordinate system, the average errors μ range from 0.5 to 0.9 pixel with standard deviations σ of 0.3 to 1.2 pixel for the image pairs between the 20 May and the 25 June. In the local coordinate system, the average errors μ range from 0.03 m to 0.11 m with standard deviations σ of 0.10 to 0.31 m for the image pairs between the 20 May and the 25 June.

4.2 Comparison with DGPS displacements

In order to estimate the accuracy and validate the calculated displacements, comparisons with independent and more accurate geodetic technique is necessary. Sixty benchmarks distributed in the stable parts and on the landslide body were monitored by DGPS with a horizontal and a vertical average accuracy of ±0.02 m and ±0.05 m. In total, 219 DGPS measurements are available for the period 2008–2009. In order to validate the displacements computed in the image plane, the DGPS benchmarks are projected in the image plane using the collinearity equations (Bonneval 1972, Kraus & Waldhaüsel, 1998). The pixel displacements derived from the image correlation are then averaged in a perimeter of 16 pixels around each benchmark. The results are presented in Figure 11A. A correlation coefficient of r=0.98 is found between DGPS measurements and Image Correlation, and an average relative accuracy of 11% is determined (Fig. 11C). In order to validate the metric displacements in the local coordinate system, the ortho-rectified displacements are averaged in an area of 4 m^2 around each benchmark and compared with the DGPS displacements. A correlation coefficient of r=0.95 is found (Fig. 11B), and an average relative accuracy of 20% is determined (Fig. 11D).

5 Discussion: sources of errors

The major sources of errors affecting the displacement calculations and thus potentially limiting the efficiency of the TOP for an operational landslide monitoring are the parameters affecting the Image Correlation computation and the external parameters influencing the ortho-rectification procedure.

5.1 Sources of errors affecting the Image Correlation computation

5.1.1 Accuracy and precision of the Image Correlation algorithm

One limitation of the Image Correlation technique is directly linked to the correlation algorithm used for matching the image pairs and to the sub-pixel interpolation method (Debella-Gilo & Kääb, 2010). The performance of a measurement system can be assessed by considering the errors associated in terms of accuracy and precision. In this section, the accuracy is represented by the average misfit between the measurements and the true value. Precision is represented by the standard deviation of the misfit between the measurements and the true value.

A series of experimental tests were carried out to assess the precision of the Image Correlation technique. The series of tests allow to investigate the influences of the size of the correlation window and of the level of noise observed in the images. Homogeneous imposed displacements (systematically equal to a multiple of pixels to avoid image resampling; Chambon & Schmittbuhl, 2003) are applied to pairs of images to create synthetic images. Furthermore, three levels of Gaussian noise were added to the original images with a mean noise level imposed to zero and variances σ^2 imposed to 10^{-4}, 10^{-3} and 10^{-2} (Fig. 12A). Then the Image Correlation technique is applied on the original image taken as reference and on the synthetic image with different sizes of correlation windows (5, 10, 16, 20, 30 and 50 pixels). For each correlation window, fifteen imposed displacements were realized with an amplitude ranging from 1 to 23 pixels along the *u* and *v*-directions. The analysis was conducted by comparing the noisy synthetic images with the reference image. In the optimal case, the measured displacement would be identical to the imposed displacement.

Each Image Correlation analysis revealed displacement differences distributed close to zero (mean accuracy of 5.10^{-4} pixels). As observed by Hild et al. (2003), the precision of the correlation algorithm mainly depends on the pixel fraction of the displacement. Larger correlation windows produce less scattered displacements and therefore improve the precision. By plotting the standard deviation of the calculated displacements against the size of the correlation window, the influence of the correlation window size can be pointed out (Fig. 12B). For very low level of noise, the precision is less than 0.1 pixel for a size of correlation window greater than 5x5 pixels. For higher level of noise, the precision is more dependent on the size of the correlation window. Because homogenous displacements field were imposed in the image, the accuracy (average misfit) is similar for small and large correlation windows. In reality, the displacement field becomes more heterogeneous at higher resolution. Therefore, an increase of the size of the

424 correlation window implies a decrease of the displacement accuracy, but, as shown in these tests,
425 an increase of the precision.

426 **5.1.2 Influence of ground surface state**

427

428 The time lag between two image acquisitions is one of the critical factors that affect the
429 correlation computation. This time has to be long enough to increase the signal (e.g. landslide
430 displacement) but short enough to preserve the tracked features (Berthier et al., 2005). Loading of
431 the snowpack on the ground during Winter, surface erosion due to fast snow melting and the
432 development of water-saturated ponds in Spring, weathering of the objects, growing of grass and
433 large deformations are environmental processes that significantly modify the surface state during
434 a year. Such correlation errors are characterized by very low correlation coefficients, very large
435 displacement amplitudes or randomly-distributed displacement directions in comparison to the
436 neighbor pixels (Fig. 13). On average, about 20 to 25% of the points are usable from one year to
437 the next year (using a correlation window of 16*16 pixels and with a correlation coefficient
438 threshold of 0.8). Consequently, the construction of long time series of displacements with the
439 image correlation technique is a difficult task for the site. The range of cumulated displacement
440 rates observed over a period of 16 months (May 2008–September 2009) is illustrated by tracking
441 the displacement at three locations in the upper (pt 1), middle (pt 2) and lower (pt 3) parts of the
442 landslide at the direct vicinity of benchmark measured by DGPS (Figs. 9, 11). In our case, the
443 cumulated displacements of the year 2009 are adjusted on those of 2008 using GCPs measured
444 with DGPS at the vicinity of the points pt1, pt2 and pt3. The monitoring of a few benchmark with
445 geodetic techniques is therefore necessary to combine displacement pattern observed in image
446 pairs acquired over the period May 2008–September 2009 (74 pairs of images). After the
447 acceleration period of Spring 2008, the displacement rates are decreasing to relative constant
448 values of about 0.02 $m.day^{-1}$ in the lower and middle parts and 0.05 $m.day^{-1}$ in the upper part
449 computed over the period July to October (Fig 14). Although these displacement rates are very
450 close to the resolution of the image, the calculated displacements are in very good agreement with
451 the displacement of the benchmarks measured by DGPS, demonstrating that the Image
452 Correlation technique is an efficient technique to complement on-site measurements.

453 **5.1.3 Influence of illumination conditions**

454 The difference observed in RGB intensities in various images acquired with various solar
455 illumination angles is an important limited factor essentially in terms of changes of the shadow

areas (Berthier et al., 2005). In order to assess the influence of illumination conditions on the image correlation results, two experiments are carried out.

The first experiment consists in correlating images acquired at different times within a day. Four photographs acquired 11:00, 12:00, 13:00 and 14:00 GMT in a period of small displacements (August 2009) and of clear sky conditions are correlated. The results indicate that illumination changes can lead to an average and a standard deviation of pixel-level error of respectively μ_{1h}=1.31 and σ_{1h}=0.03, μ_{2h}=1.35 and σ_2 =0.12, μ_{3h}=1.89 and σ_{3h}=0.18 pixel for time-interval acquisition of respectively 1, 2 and 3 hours. The results demonstrate that the correlation of images acquired in nearly similar illumination conditions can display a pixel-level precision.

The effect of illumination changes can be larger if the images are acquired at different seasons. This influence cannot be assessed by correlating images distant in time because of the landslide displacements. Therefore the second experiment consists in creating synthetic images with different shadow areas as a function of the sun azimuth and elevation (Burrough & McDonell, 1988). Only the shadows created by direct solar illumination are analyzed assuming clear-sky conditions; the effects of reflected and diffuse illuminations are neglected. First, the shaded relief on the landslide is computed from the DEM in the local coordinate system. Then, the shaded relief is projected and linearly interpolated in the image plane coordinate system. 97 shaded relief images were created with different artificial illuminations. An example of shaded relief image is represented in Figure 5. Because a preference is given to correlate images taken when the sun elevation is maximal (Delacourt et al., 2007), a shaded relief image with a sun elevation of 65° and a sun azimuth of 250° (illumination coming from the South-West) is chosen as the reference image for the correlation. It represents the illumination conditions on the landslide in the month of July at 12:00 GMT in clear sky conditions. The reference image is correlated with the shaded relief images, and the calculated displacements are compared to the errors induced by illumination changes. The mean displacement error and the mean correlation coefficient are used to characterize the influence of illumination changes on the image. Because only the shadow intensities are correlated, the errors are overestimated and are therefore represented by a normalized index.

As expected, the correlation of the synthetic images show that the correlation coefficient tends rapidly to r=1 when the sun elevation is closer to the reference image (at 12.00 GMT) and the slope of the relationship depends on the sun azimuth (Fig. 15A). At the opposite, the correlation coefficient drops quickly when the illumination comes from the South-East (azimuth of 120°) and shows a strong sensitivity to sun elevation changes. Low sun azimuth (120°) and low elevation angles (30°) typically represent illumination conditions at the end of the daytime which are thus

not optimal for the correlation. In addition, low sun elevations (30°) and higher azimuths (200°) are typical illumination conditions of the autumn period at 12.00 GMT. These images are also not very relevant for the calculation of the displacements because the correlation coefficient is low. This finding is in agreement with Table 2 which indicates the amount of interpretable displacements is lower in the autumn season than in the summer season (lower correlation coefficients).

Figure 15B presents the mean correlation coefficient versus the displacement noise index. As expected, for sun azimuths equal to the reference image (240°), the displacement noise decreases with an increase of the correlation coefficient. In very bad illumination conditions (e.g. a low sun elevation and a sun azimuth opposite to the reference -100°-), the trend is inversed because the image becomes very low textured (most areas of the landslide are in the shadow with homogeneous intensity values). In that case, no maximum correlation value is computed, resulting in a null displacement with the correlation algorithm used in this study. Similar results are observed for images displaying homogeneous texture such as for instance in backlighting conditions, in foggy meteorological conditions or when the ground surface is covered by snow.

Therefore, correlation of images with a too important time-lapse has to be avoided to minimize illumination effects. A possible alternative is to correlate images under diffused illumination (cloudy day) thus providing a more homogenous lightning. At the opposite, correlation of images acquired at the same solar time in the day and when the sun elevation is maximal is optimal.

5.2 Sources of errors affecting the ortho-rectification procedure

5.2.1 Influence of camera orientation

The accuracy camera orientation is a parameter affecting both the image geometry and the accuracy of the geo-referencing (Mikhail et al., 2001). If changes in external orientations of the camera are small, the image geometry is not significantly affected. Consequently a homogeneous component in the correlated displacement field is visible in the image plane (Fig. 16A). This misfit can be significant in the areas where the expected displacements are low or null such as in the stable parts. This systematic error can be corrected assuming a rigid translation of the image by removing the average Δu and Δv misfits (observed on the stable parts of the images such as stable crests or on reference targets located outside the landslide; Fig. 2B, A; Fallourt et al., 2010). Nevertheless this correction is not fully optimal, because the geometric deformations caused by the slight orientation changes of the camera depend on the object distance. Therefore,

521 after correction of the homogeneous component in the image plane, an average residual misfit of
522 about 0 to 2 pixels is observed .
523 In order to evaluate the accuracy of the external orientation that influences the georeferencing
524 quality, fourty GCPs not introduced in the minimization processes of section §3.2.3 are used. The
525 shift between the projected and the observed GCPs positions in the image plane is thus
526 determined (Fig. 16B). A mean shift error of, respectively, -0.20 and -0.08 pixel with a standard
527 deviation of 1.59 and 1.51 pixels in the *u* and *v*-directions respectively is obtained (Table 4). The
528 accuracy of the external parameters in the georeferencing procedure in the local coordinate
529 system is calculated by comparing the back-projected GCPs identified in the image plane with the
530 GCPs positions measured with DGPS and located in the stable parts. The absolute accuracy in *X,*
531 *Y* and *Z* coordinates are presented in Table 4. Because most of GCPs in the stable parts are
532 located in the background of the image (750 m from the camera location) where the ground pixel
533 size is about 20 cm, the mean 3D error (0.14 m) and the standard deviation (0.56 m) of the
534 positioning are not representative of the areas of the landslide located closer to the camera
535 (300 m). Nevertheless, because the standard deviation of the GCP located in the image plane are
536 close to the accuracy of the GCPs picking, the determination of the camera orientation is
537 considered acceptable. Furthermore, the good coherence between the shaded relief images
538 (Fig. 5) and the true images (Fig. 2A) shows that the quality of the determination of the camera
539 orientation is satisfying.

540 **5.2.2 Influence of the DEM**

541 The accuracy of the DEM used in the ortho-rectification procedure is important to correct large
542 distortion induced by the topography, which in turn controls the accuracy of the displacements in
543 the local coordinate system. Therefore, the actual necessity of using a mono-temporal DEM for
544 the complete series of image pairs has to be addressed. In order to evaluate its influence on the
545 ortho-rectified displacements, the displacements of the 1st June–4th June 2008 originally ortho-
546 rectified with the DEM of October 2007 (Fig. 9) are compared with those orthorectified with the
547 DEM of July 2009 documenting a slightly different landslide morphology (Fig. 17A, B). The
548 observed differences in displacement are presented relative to the displacement orthorectified
549 with the DEM of 2007. The differences vary spatially in the landslide area. Despite some areas
550 displaying differences in displacement larger than 75%, the average difference is 21% which is
551 very similar to the differences observed with the DGPS measurements (Fig. 11D). As a
552 consequence, the influence of the DEM on the accuracy of the displacement is more important
553 than the influence of the camera orientation, the image resolution and changes in illumination

554 conditions. For large displacements, morphologic changes become significant and the errors on
555 the displacements increase. The computation of multi-temporal DEMs for each image is therefore
556 a pre-requisite to improve the accuracy of the ortho-rectified displacements. Nevertheless, in case
557 of a translational landslide characterized by low changes in elevation, the use of the same DEM
558 constitutes still an acceptable 1st-order estimate.
559

560 # 6 Conclusion

561 The potential of multi-temporal correlation of ground-based images for landslide monitoring has
562 been assessed using the dataset available on the Super Sauze landslide (South French Alps). A
563 methodology to compute displacement rates both in the image plane coordinate system and in the
564 local coordinate system has been proposed.
565 The results demonstrated clearly the potential and the limitation of this technique by identifying
566 the heterogeneous displacement field, in space and in time, of the landslide. The camera
567 monitoring allowed to characterize displacements up to 3 m.day^{-1} during an acceleration period,
568 and displacement of about 0.02 m.day^{-1} computed over the period July to September (the less
569 active period). The results are in good agreement with previous knowledge on the landslide
570 kinematics and are in very good agreement with benchmark displacements measured by DGPS.
571 For objects located in a range of 300 to 900 m from the camera location, this study showed that
572 the pixel size can vary from 0.005 to 0.04 m^2 according to the resolution of the image (2000x3008
573 pixels) and the angle of incidence of the line of sight. The orientation of the line of sight
574 (depending on the location and orientation of the camera) to the ground surface has to be
575 considered before installing a permanent monitoring system. Areas of low incidence angles (< 5°)
576 are very sensitive to small movements of the camera. Therefore, the angle should be the most
577 perpendicular as possible to the mean displacement vector of the landslide. 3D displacements of
578 less than 0.04 m and 0.06 m in the lower part of the landslide and 0.09 m and 0.11 m in the *u* and
579 *v*-directions are difficult to measure over a period of four days without a sub-pixel correlation
580 algorithm.
581 The strongest limitations are independent of the acquisition system and are related to the
582 meteorological and illumination conditions and the ground surface changes inducing partial or
583 complete loss of coherence between pairs of images. During the winter season (from November
584 to May), the presence of snow impedes reliable correlation results and excessive ground
585 deformations between two consecutive years impede valid displacement measurements even if
586 the images are acquired during the same solar time. The small changes in the camera orientation

and the use of a constant DEM are the most important parameters that affect the accuracy of the ortho-rectification of the displacement field. A regular acquisition of multi-temporal DEMs through airborne or terrestrial laser scanning or stereoscopic photogrammetric views is believed to be a priority to significantly improve the accuracy of the technique. The errors induced by the sub-pixel correlation algorithm are thus insignificant compared to the influences of the other parameters cited previously.

The results demonstrate that Image Correlation techniques implemented in permanent monitoring system is particularly interesting for monitoring landslides characterized by annual pluri-decimetric displacements. In addition, this low cost technique is a very suitable alternative for inaccessible landslides or areas without access to power supply. Furthermore, because the proposed methodology does not require GCPs except for determining the external orientation of the camera and for combining displacement pattern observed in image pairs acquired over two years, the methodology can be routinely and automatically applied to new pairs of images. Therefore this study offers very promising perspectives for operational applications which can be potentially integrated in an early warning system by considering additional efforts in direct data transmission. Finally, inversion of the displacement field could be developed to characterize the macroscopic rheological properties of the landslide material.

Acknowledgements

This work was supported by the European Commission within the Marie Curie Research and Training Network '*Mountain Risks: from prediction to management and governance*' (2007-2010, Contract MCRTN-035798) and by the FP7 Large-scale Integrating Project '*Safeland: Living with landslide risk in Europe*" (2009-2012, Contract 226479). The ortho-images and the airborne LiDAR data of the Super-Sauze landslide have been acquired by the Helimap System service in 2009. The authors would like to acknowledge André Stumpf (University of Strasbourg, France & University of Twente, Netherlands) and Sabrina Rothmund (University of Stuttgart, Germany) for their help in the field. Special thanks are also due to Bas van Dam (Utrecht University, Netherlands) who designed the automatic monitoring system.

References

618 Alaoui El. M. I., & Ibn-Elhaj E. (2009). A robust hierarchical motion estimation algorithm in
619 noisy image sequences in the bispectrum domain. *Signal Image and Video Processing, 3,*
620 291-302.
621 Anandan, P., Bergen, R.J., Hanna, K.J., & Hanna, K.J. (1993). Hierarchical model-based motion
622 estimation. In L. Sezan, (Eds.), *Image Sequence Analysis*. Kluwer, Dordrecht.
623 Antonello, G., Casagli, N., Farina, P., Leva, D., Nico, G., Sieber, A.J., & Tarchi, D. (2004).
624 Ground-based SAR interferometry for monitoring mass movements. *Landslides, 1,* 21-28.
625 Baratoux, D., Delacourt, C., & Allemand, P. (2001). High-resolution digital elevation models
626 derived from Viking Orbiter images: Method and comparison with Mars Orbiter Laser
627 Altimeter Data. *Journal of Geophyscal Research, 106,* 32927-32941.
628 Bastard M., (2009). Caractérisation de la cinématique de glissement de terrain par technique de
629 correlation d'image optique. Master thesis. University of Strasbourg (EOST). Institut de
630 Physique du Globe, Strasbourg, France.
631 Berthier, E, Vadon, H., Baratoux, D., Arnaud, Y., Vincent, C., Feigl, K. L., Rémy, F., & Legrésy
632 B. (2005). Surface motion of mountain glaciers derived from satellite optical imagery.
633 *Remote Sensing of Environment, 95,* 14-28.
634 Besl, P., & McKay, N. (1992). A method for registration of 3-D shapes. *IEEE Transactions on*
635 *Pattern And Machine Intelligence, 14,* 239-256.
636 Bitelli G., Dubbini M., & Zanutta A. (2004). Terrestrial laser scanning and digital
637 photogrammetry techniques to monitor landslides bodies, *International Archives of*
638 *Photogrammetry, Remote Sensing and Spatial Information Sciences 35*, 246–251.
639 Bonneval, H., (1972). Levés topographiques par photogrammétrie aérienne. In Eyrolles (Eds.),
640 *Photogrammétrie générale: Tome 3, Collection scientifique de l'Institut Géographique*
641 *National*, Paris, France.
642 Brunner, F., Macheiner, K., & Woschitz, H. (2007). Monitoring of deep-seated mass movements.
643 *Proceedings of the 3rd International Conference on Structural Health Monitoring of*
644 *Intelligent Infra-structure*, Vancouver, Canada.
645 Burrough, P. A., & McDonell, R.A. (1998). *Principles of Geographical Information Systems*
646 ,Oxford University Press, New York.
647 Casagli, N., Farina, P., Leva, D., & Tarchi, D. (2004). Application of ground-based radar
648 interferome-try to monitor an active rock slide and implications on the emergency
649 management. In E. Kluwer (Eds.), *The NATO Advanced Research Workshop*, Celano, Italy.
650 Casson, B., Baratoux, D., Delacourt, D., & Allemand, P. (2003). "La Clapière" landslide motion
651 observed from aerial differential high resolution DEM. *Engineering. Geology, 68,* 123-139.

652 Casson B., Delacourt C., & Allemand, P. (2005). Contribution of multi-temporal sensing images
653 to characterize landslide slip surface – Application to the La Clapière Landslide (France).
654 *Natural Hazards and Earth System Sciences, 5,* 425-437.
655 Cardenal, J., Mata, E., Perez-Garcia, J.L., Delgado, J., Andez, M.A., Gonzalez, A., Diaz-de-
656 Teran, J.R. (2008). Close Range Digital Photogrammetry Techniques applied to Landslide
657 Monitoring. International Archives of the Photogrammetry, *Remote sensing and Spatial*
658 *Information Sciences*. Vol XXXVII. Part B8.
659 Chambon G. (2003). Caractérisation expérimentale du frottement effectif des zones de faille. PhD
660 Thesis. Université Paris XI Orsay, ENPC..
661 Chambon, G., & Schmittbuhl, J. (2003). Shear with comminution of a granular material:
662 Microscopic deformations outside the shear band. *Physical Review E, 68,* 1-8.
663 Corripio, J.G. (2004). Snow surface albedo estimations using terrestrial photography.
664 *International Journal of Remote Sensing, 25(24),* 5705-5729.
665 Corsini, A., Farina P., Antonello G., Barbieri M., Casagli N., Coren F., Guerri L., Ronchetti F.,
666 Sterzai P., & Tarchi D. (2006). Space-borne and ground-based SAR interferometry as tools
667 for landslide hazard management in civil protection. *International Journal of Remote*
668 *Sensing, 27,* 2351 - 2369.
669 D'Antone, I. (1995). Hierarchical correlation for track finding. *Nuclear Instrument and Methods*
670 *in Physics Research, 356,* 476-484.
671 Debella-Gilo M., & Kääb A. Sub-pixel precision image matching for measuring surface
672 displacements on mass movements using normalized cross-correlation. *Remote Sensing of*
673 *Environment* (2010).
674 Delacourt, C., Allemand P., Casson B., & Vadon H. (2004). Velocity field of the "La Clapiere"
675 landslide measured by the correlation of aerial and Quick-Bird satellite images. *Geophysical.*
676 *Research Letters, 31,* 1-5.
677 Delacourt, C., Allemand, P., Berthier, E., Raucoules, D., Casson, B., Grandjean, P., Pambrun, C.,
678 & Varel, E. 2007. Remote-sensing techniques for analysing landslide kinematics: a review.
679 *Bulletin de Société Géologique, 178,* 89-100.
680 Fallourd, R., Vernier, F., Friedt J.-M., Martin, G., trouvé, E., Moreau, L. & Nicolas, J.-M. (2010).
681 Monitoring temperate glacier with high resolution automated digital cameras – Application to
682 the Argentière Glacier. in: Paparoditis N., Pierrot-Deseilligny M., Mallet C.& Tournaire O.
683 (Eds.), IAPRS, Vol. XXXVIII, Part 3B, Saint-Mandé, France., 1-23.
684 Fisher, P.F. (1991). First experiments in viewshed uncertainty: The accuracy of the viewshed
685 area. *Photogrammetric Engineering Remote Sensing, 57,* 1321-1327.

686 Foppe, K., Barth, W., & Preis, S. (2006). Autonomous Permanent Automatic Monitoring System
687 with Robot-Tacheometers. *Proceedings of* of the XXIII International FIG Congress, Munich,
688 Germany.
689 Franklin, W.R., & C.K. Rav. (1994). Higher isn't necessarily better: Visibility algorithms and
690 experiments, *Proceedings of-the 6th International Symposium on Spatial Data Handling*,
691 Edinburgh, Scotland, 2, 751-770.
692 Heikkila, J., & Silven, O. (1997). A four-step camera calibration procedure with implicit image
693 correction. *IEEE Computer. Society*, 1106-1112.
694 Hemmleb, M., & Wiedemann, A. (1997). Digital Rectification and Generation of Orthoimages in
695 Architectural Photogrammetry. *CIPA International Symposium*, IAPRS, XXXII, Part 5C1B
696 (pp. 261-267), Göteborg, Sweden.
697 Hild F. (2003). Mesure de champs de déplacement par corrélation d'images et applications en
698 mécanique des solides. *Notes de cours IPSI*. Laboratoire de Mécanique et Technologie,
699 CNRS-UMR 8535, Université Paris 6, France.
700 Honda, K., & M. Nagai (2002), Real-time volcano activity mapping using ground-based digital
701 imagery, *ISPRS Journal of Photogrammetry and Remote Sensing, 57,1-2,* 159-168.
702 Jaboyedoff M., Ornstein P., & Rouiller J.-D. (2004). Design of a geodetic database and associated
703 tools for monitoring rock-slope movements: the example of the top of Randa rockfall scar.
704 *Natural Hazards and Earth System Science, 4,* 187-196.
705 Jaboyedoff, M., Oppikofer T., Abellan A., Derron M.-H., Loye A., Metzger R., & Pedrazzini A.
706 (2010). Use of LiDAR in landslide investigations : a review. *Natural Hazards.* doi
707 10.1007/s11069-010-9634-2
708 Jiang, R., Jauregui, D.V., & White, K. (2008). Close-range photogrammetry applications in
709 bridge measurement: Literature review. *Measurement, 41,* 823-834.
710 Kraus, K. & Waldhäusl, P., (1994). *Photogrammetry, Fundamentals and Standard processes*. vol
711 1. Hermès (editor), Paris.
712 Kumar, S., & Banerjee, S., (1998). Development and application of a hierarchical system for
713 digital particle image velocimetry to free-surface turbulence. *Physics of Fluids, 10,* 160-177.
714 Küntz, M., Jolin, M., Bastien, J., Perez F., & Hild, F. (2007). Digital image correlation analysis of
715 cracks behavior in a reinforced concrete beam during a load test. *Canadian journal of civil*
716 *engineering, 33*, 1418-1425.
717 LePrince, S., Berthier, E., Ayoub, F., Delacourt, C., & Avouac, J.- P. (2008). Monitoring Earth
718 Surface Dynamics With Optical Imagery. *Eos,* 89, 1-5.
719 Lewis, J.P., (1995). Fast normalized cross-correlation. Vision Interface, 120-123.

720 Lim, M., Petley, D.N., Rosser, N.J., Allison, R.J., Long, A.J. & Pybus, D. (2005). Combined
721 digital photogrammetry and time-of-flight laser scanning for monitoring cliff evolution. *The*
722 *Photogrammetric Record*, 20, 109-129.
723 Luzi, G., (2010). Ground based SAR interferometry: a novel tool for Geoscience. In:
724 Geoscience and Remote Sensing, New Achievements, P.Imperatore & D. Riccio (Editors),
725 ISBN: 978-953-7619-97-8. In print.
726 Malet, J.-P., Maquaire, O., & Calais, E. (2002). The use of global positioning system techniques
727 for the continuous monitoring of landslides. *Geomorphology, 43,* 33-54.
728 Malet, J.-P. (2003). Les glissements de type écoulement dans les marnes noires des Alpes du Sud.
729 Morphologie, fonctionnement et modélisation hydromécanique. PhD Thesis in Earth
730 Sciences, Université Louis Pasteur, Strasbourg.
731 Mantovani, F. Soeters R., & van Western C.J. (1996). Remote sensing techniques for landslide
732 studies and hazard zonation in Europe. *Geomorphology, 15,* 213-225.
733 Maas, H.-G., Schwalbe, E., Dietrich, R., Bässler, M., & Ewert, H. (2008). Determination of
734 spatio-temporal velocity fields on glaciers in West- Greenland by terrestrial image sequence
735 analysis. *IAPRS*, XXXVII, Part B8 Beijing,China, 1419-1424.
736 Meissl, A., & Naterop, D. (1995). Automatic Measuring System for Permanent Monitoring –
737 Solexperts GeoMonitor. *Proceedings of Field Measurements in Geomechanics 4th*
738 *International Symposium*, Bergamo, Italy, 489-494.
739 Mikhail, E., Bethel, J. S., & McGlone, J. C. (2001). *Introduction to Modern Photogrammetry*,
740 Hardcover (edition), New-York.
741 Monserrat, O., & Crosetto, M. (2008). Deformation measurement using terrestrial laser scanning
742 data and least squares 3D surface matching. *ISPRS Journal of Photogrammetry and Remote*
743 *Sensing, 63*, 142-154.
744 Moore J.F.A. (1992). Monitoring Building Structures. Blackie & Son Ltd. 155 p. ISBN 0-216-
745 93141-X.
746 Oppikofer T., Jaboyedoff M., & Kreusen H-R. (2008). Collapse at the eastern Eiger flank in the
747 Swiss Alps. *Nature Geoscience, 8,* 531-535.
748 Pesci A., Baldi B., Bedin A., Casula G., Cenni N., Fabris M., Loddo F., Mora P., & Bacchetti M.
749 (2004). Digital elevation models for landslide evolution monitoring: application on two areas
750 located in the Reno River Valley (Italy). *Annals of Geophysics, 47,* 1339-1353.
751 Prokop, A., & Panholzer, H. (2009). Assessing the capability of terrestrial laser scanning for
752 monitoring slow moving landslides. *Natural Hazards and Earth System Sciences, 9,* 1921-
753 1928.

754 Rohaly J., Frigerio F., & Hart D. P. (2002). Reverse hierarchical PIV processing. *Measurement*
755 *Science and Technology, 13,* 984-996.
756 Squarzoni C., Delacourt C., & Allemand P. (2005). Differential single-frequency GPS monitoring
757 of the La Valette landslide (French Alps). *Engineering Geology, 79,* 215-229.
758 Sturzenegger, M., & Stead, D. (2009). Close-range terrestrial digital photogrammetry and
759 terrestrial laser scanning for discontinuity characterization on rock cuts. *Engineering*
760 *Geology, 106,* 163-182.
761 Tarchi, D., Casagli, N., Fanti, R., Leva, DD., Luzi, G., Pasuto, A., Pieraccini, M., & Silvano, S.
762 (2003). Landslide monitoring by using ground-based SAR interferometry: an example of
763 application to the Tessina landslide in Italy. *Engineering Geology, 68,*15-30.
764 Teza, G., Galgaro, A., Zaltron, N., & Genevois, R. (2007). Terrestrial laser scanner to detect
765 landslide displacement fields: a new approach, *International Journal of Remote Sensing, 28,*
766 3425-3446.
767 Teza, G., Pesci, A., Genevois, R., & Galgaro, A. (2008). Characterization of landslide ground
768 surface kinematics from terrestrial laser scanning and strain field computation.
769 *Geomorphology, 97,* 424– 437.
770 Travelletti, J & Malet, J-P. Characterization of the 3D geometry of flow-like landslides: a
771 methodology based on the integration of multi-source data. *Submitted in Engineering*
772 *Geology*.
773 Wangensteen, B., Guomundsson, A., Eiken, T., Kääb, A., Farbrot, H., & Etzelmüller, B. (2006).
774 Surface displacements and surface estimates for creeping slope landforms in Northern and
775 Eastern Iceland using digital photogrammetry. *Geomorphology, 80*, 59-79.
776 White, D. J., Take, W. A. & Bolton, M. D., (2003). Soil deformation measurement using particle
777 image velocimetry (PIV) and photogrammetry. *Géotechnique, 53,* 619-631.

Figure(s) & Tables(s)
Click here to download Figure(s): IJPRS-Travelletti_et al_SUBMITTED-VERSION_figures_tables.pdf

Figures

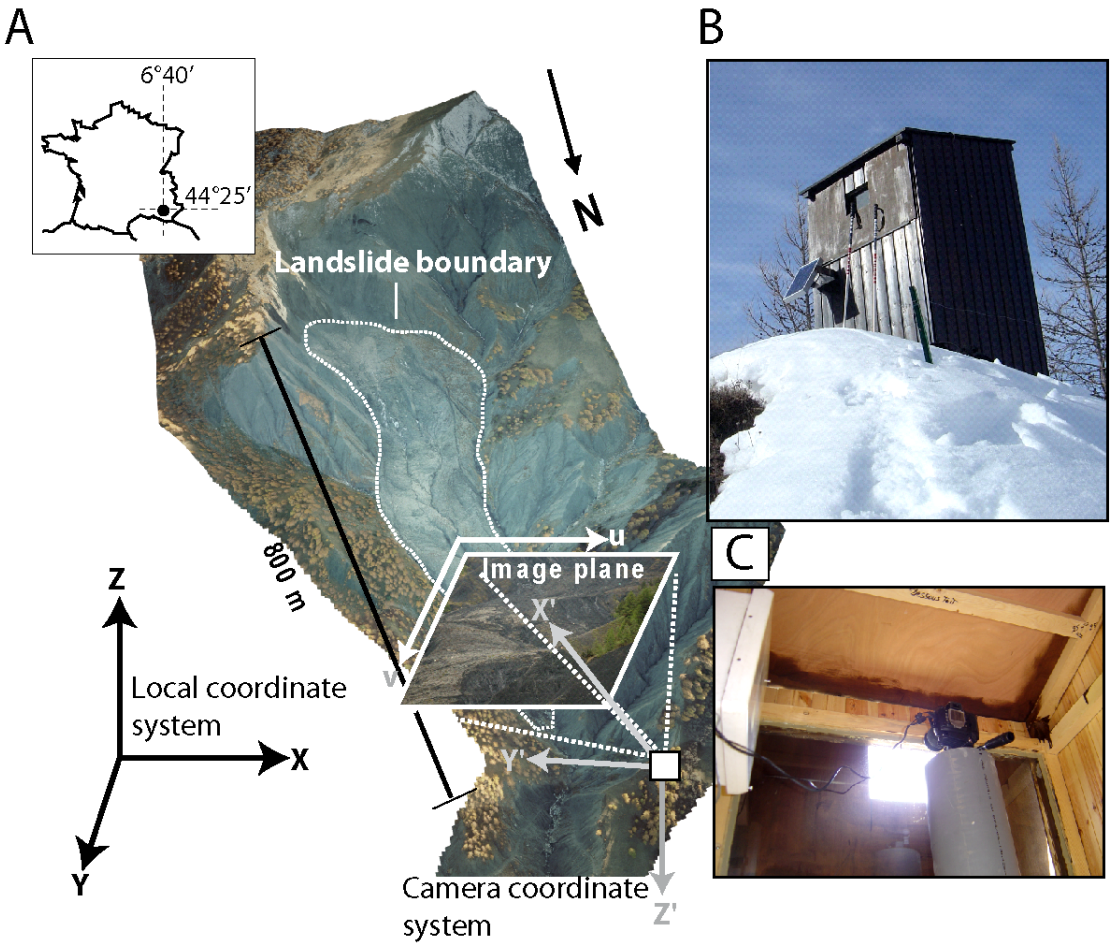


Fig. 1. (A) View of the Super-Sauze landslide towards the south with the different coordinate systems used in the georeferencing procedure. (B) Location of the camera monitoring system (C)

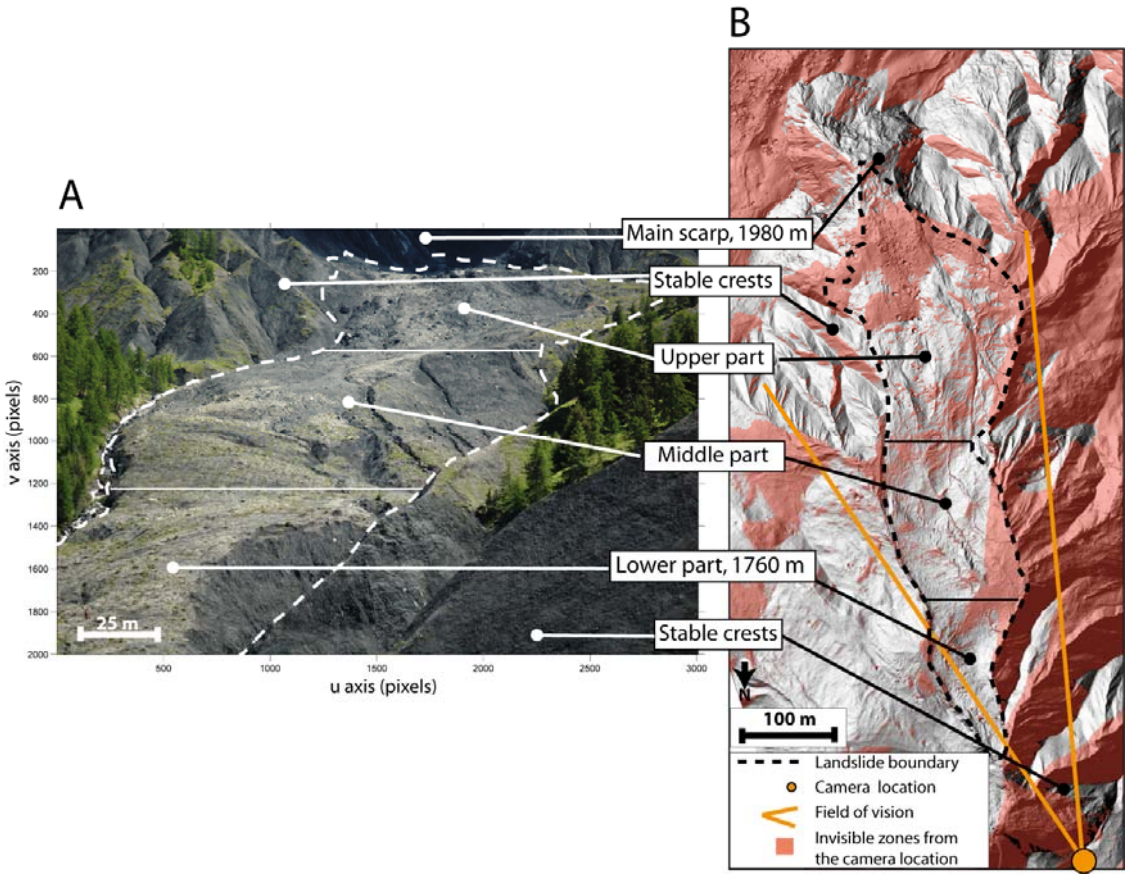


Fig. 2. Views of the landslide in the image geometry and in the local coordinate system (A) Image acquired by the monitoring system showing the different parts of the landslide from the camera location. (B) View of the landslide morphology in the local coordinate system on a shaded relief computed with a 0.25 m mesh DEM interpolated from airborne-LiDAR data sets acquired in July 2009. The invisible areas from the camera location are also shown.

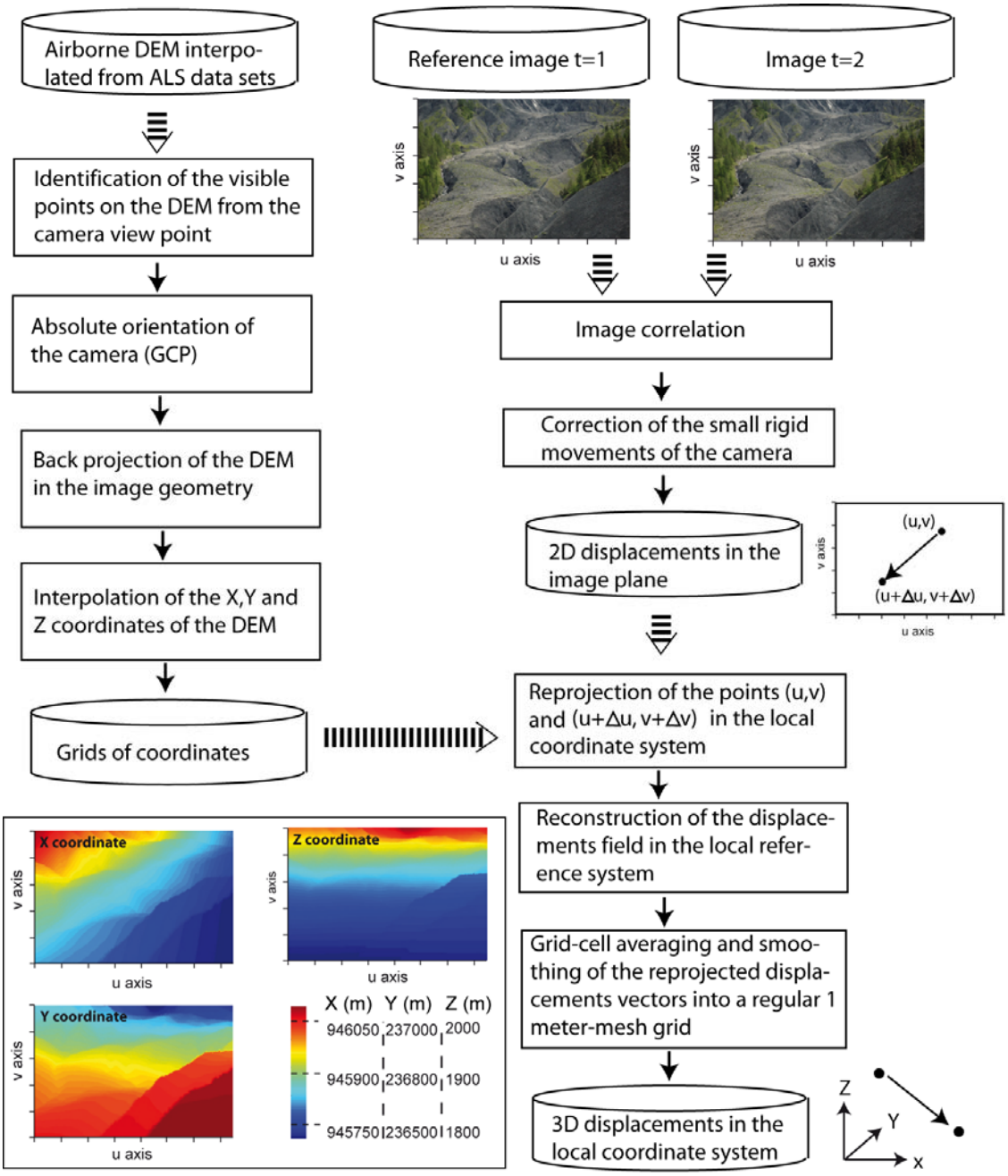


Fig 3. Flowchart of the methodology

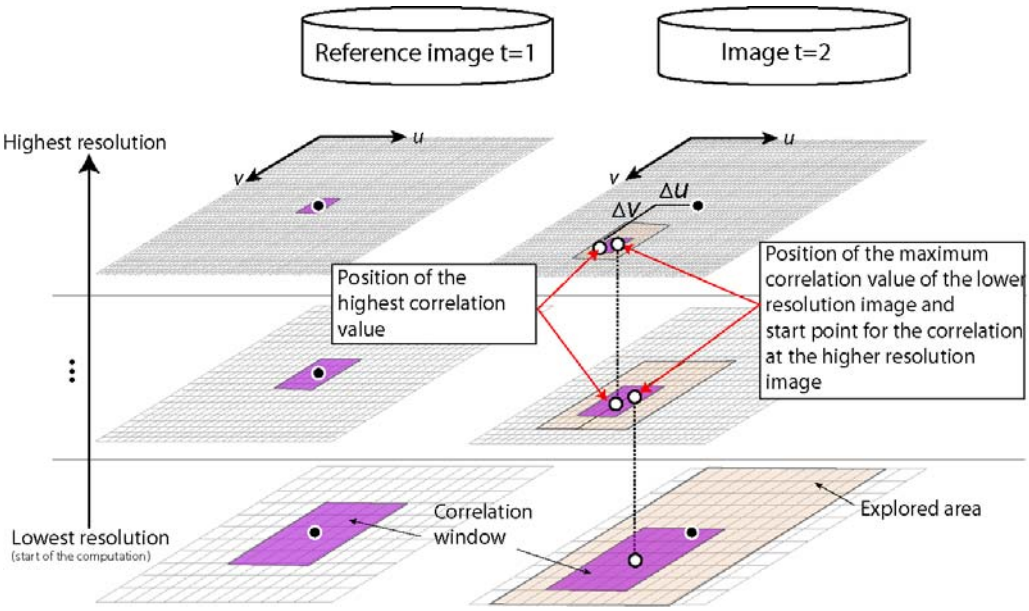


Fig. 4. Principle of the normalized hierarchical image correlation. The correlation computation starts from the lowest resolution to the highest resolution by keeping constant the size of the correlation window and the explored area, while their physical size is decreasing. At each higher resolution level, the explored area is centered on the pixel with the highest t correlation value of the previous resolution level. The estimate of the position of the maximum correlation value is thus increased.

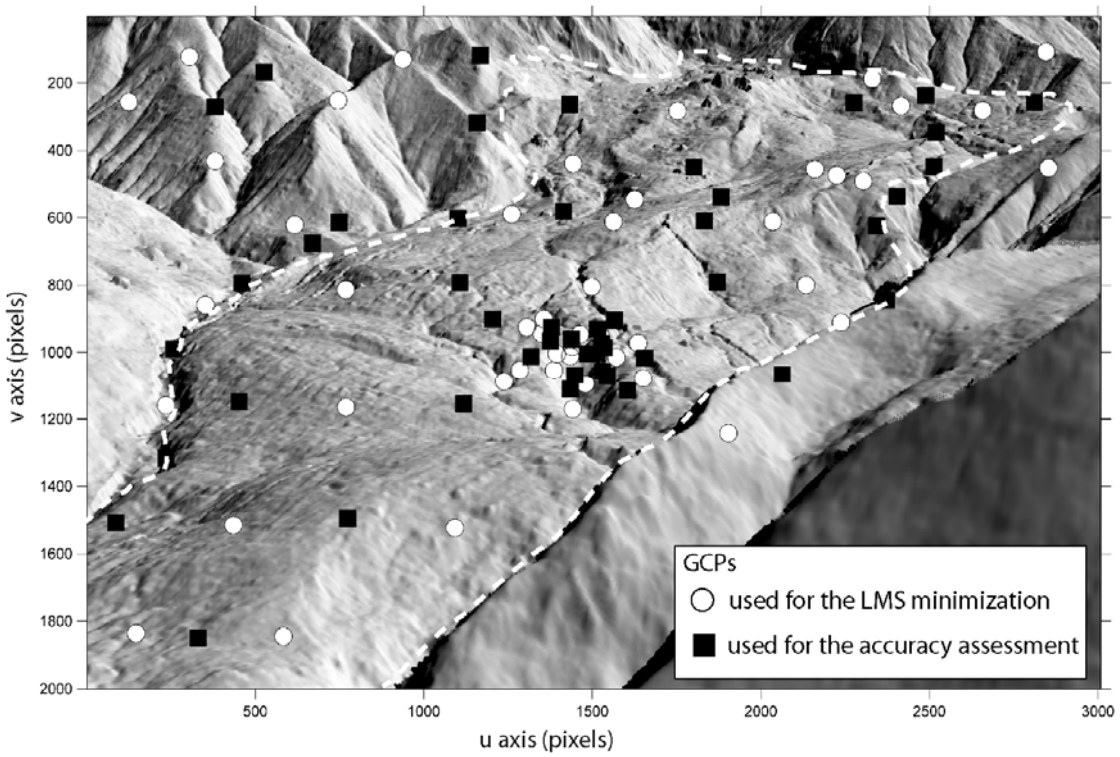


Fig.5. Location of the GCPs used for the Least Mean Square minimization (LMS) and for the accuracy analysis in a shaded relief image. The shaded relief image is produced by interpolating the shaded relief values of the DEM of 2009 projected in the image plane. This image is useful to visually check the quality of the back projection by comparison with a real image.

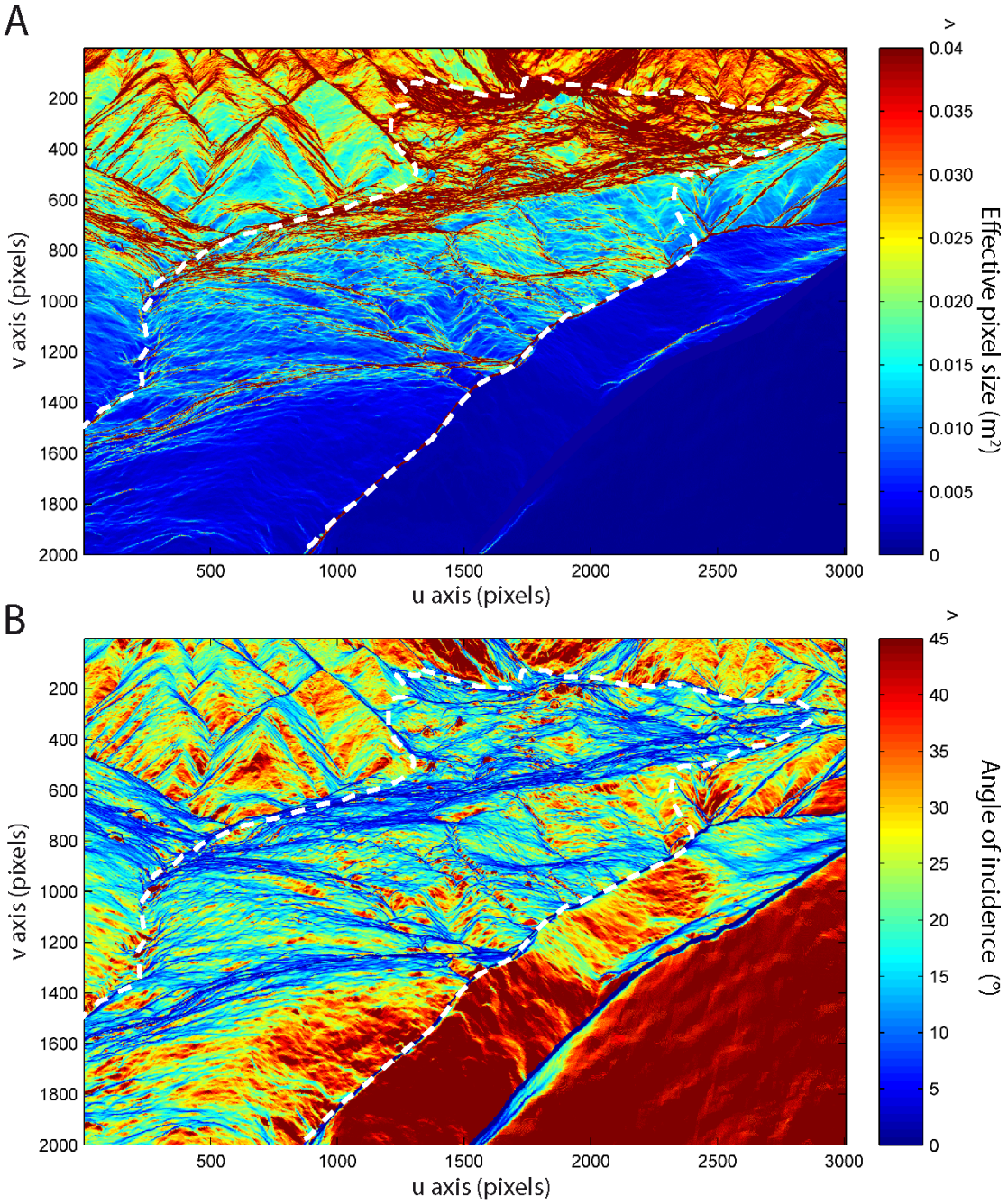


Fig. 6. Image resolution characteristics: (A) Effective pixel size in square meters (B) Angle of incidence in degrees. A low angle means that the line of sight is nearly tangential to the topography.

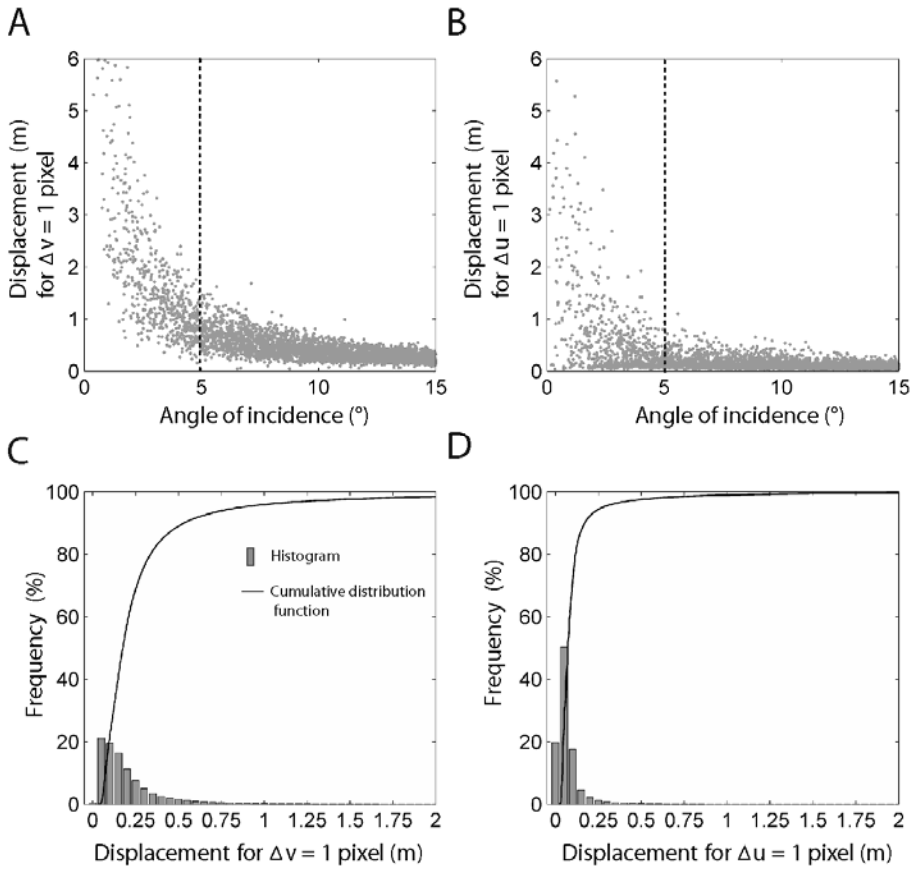


Fig. 7. Minimum metric displacement for pixel accuracy in v-axis (A) and u-axis (B) according to the angle of incidence. The sensitivity of metric displacements to small changes in u and v directions drastically increases for angle of incidence below 5°. (C) and (D) histograms and cumulative distribution function of the metric displacements resulting for 1 pixel displacement in v-axis and u-axis. 50% of the pixels in the image plane inside the landslide area shows a metric sensitivity less than 0.17 m for 1 pixel displacement in v-axis and 0.07 m in u-axis.

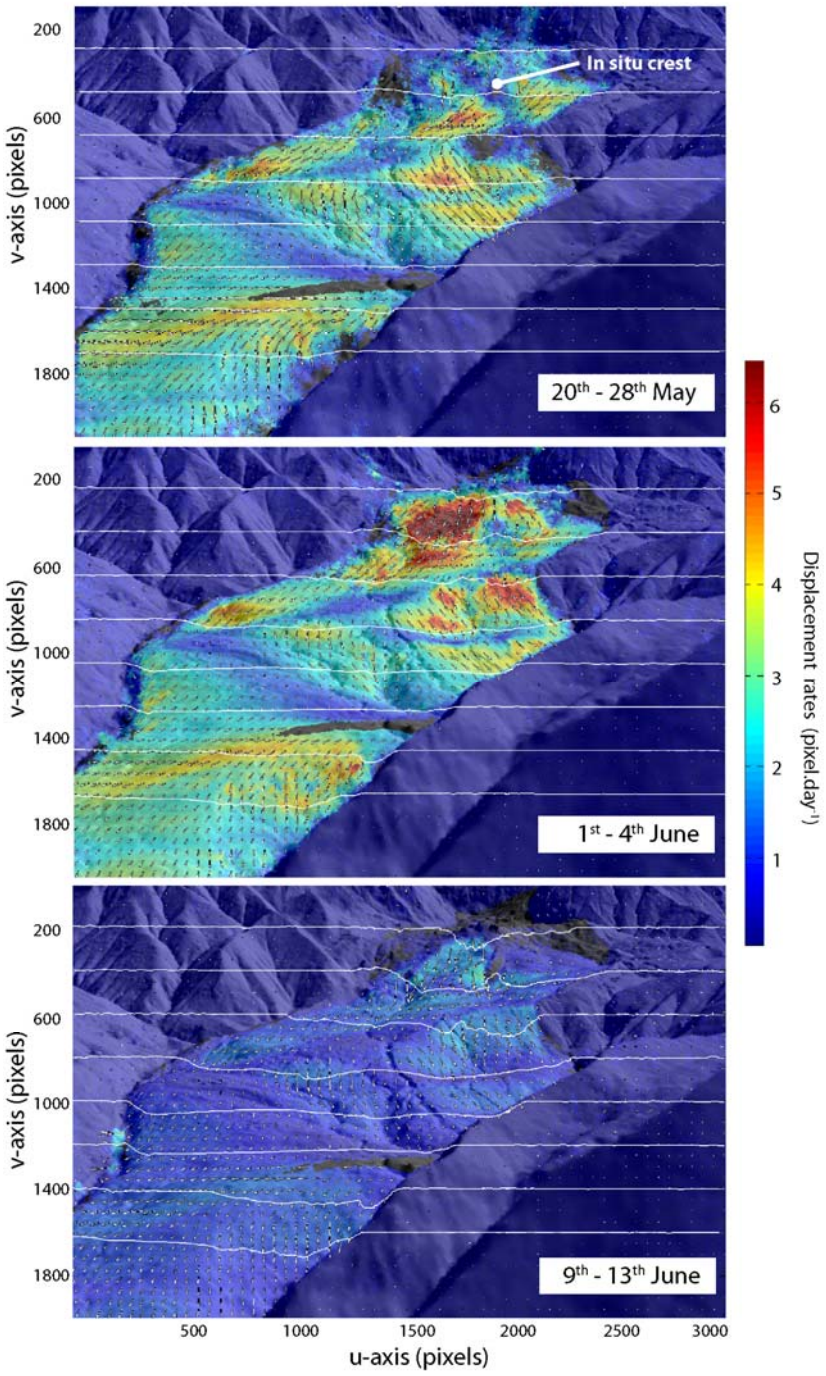


Fig. 8. Displacement rates amplitude (color) and displacement direction (arrows) in the image plane and cumulated displacements along 8 profiles crossing the landslide over the period the 20^{the} May to the 25^{the} June 2008. In order to highlight the displacement direction, the arrow length is normalized in each image.

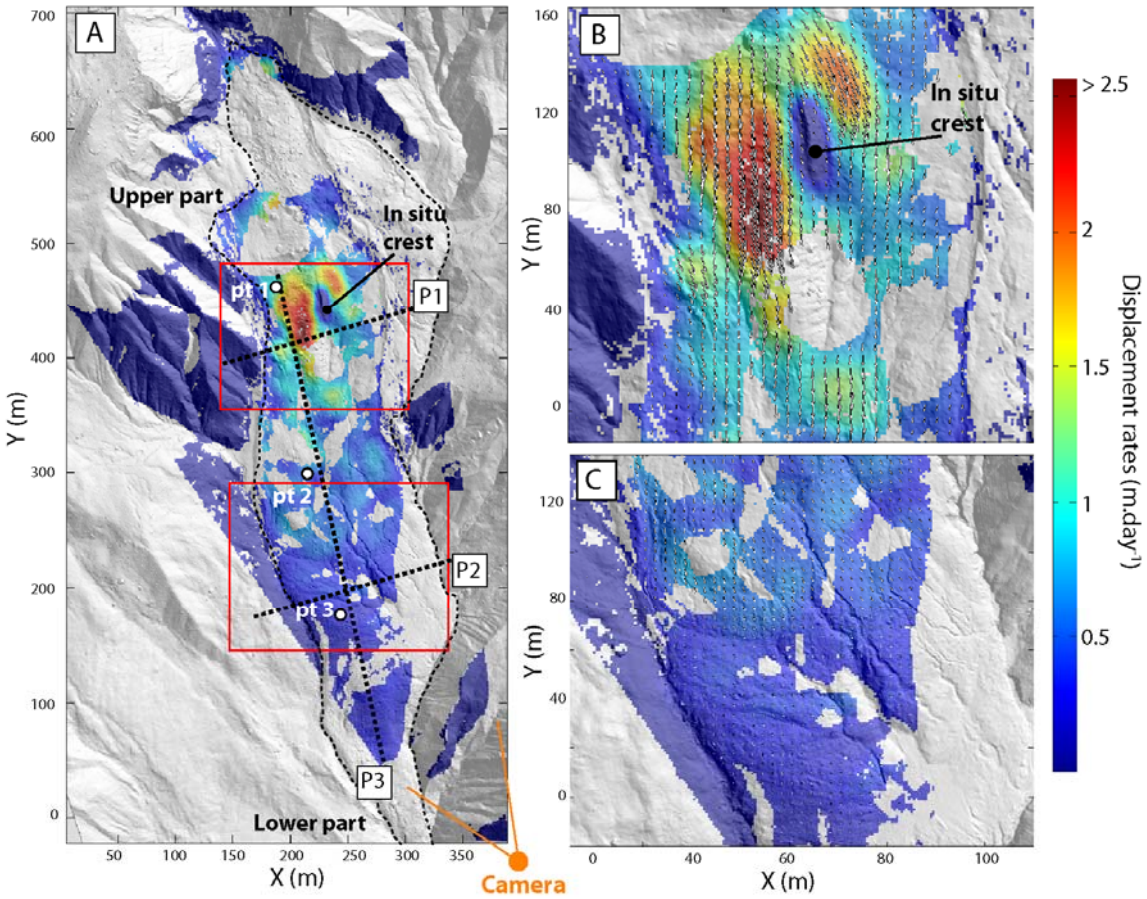


Fig. 9. Displacement rates map for the period 1st – 4th June 2008. (A) Displacement rates observed on the whole landslide. The profiles P1, P2 and P3 refer to Fig. 10 and the locations pt 1, pt 2 and pt 3 refer to Fig. 11. (B) Details on the displacement rates and displacement direction of the velocity amplitude and direction in the upper part. (C) Details on the displacement rates and displacement direction in the lower part.

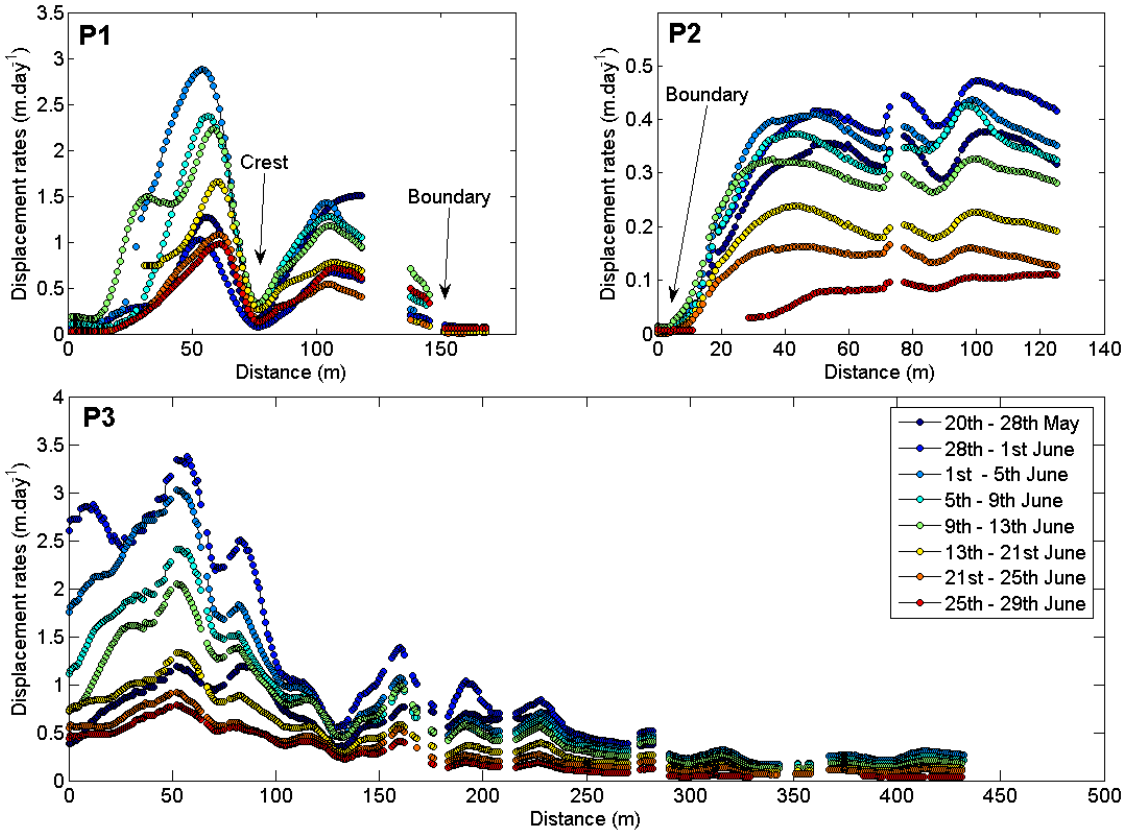


Fig. 10. Displacement rates profiles in the upper (P1), the medium (P2) and the lower (P3) part of the landslide. The location of the profiles is indicated in Fig. 9.

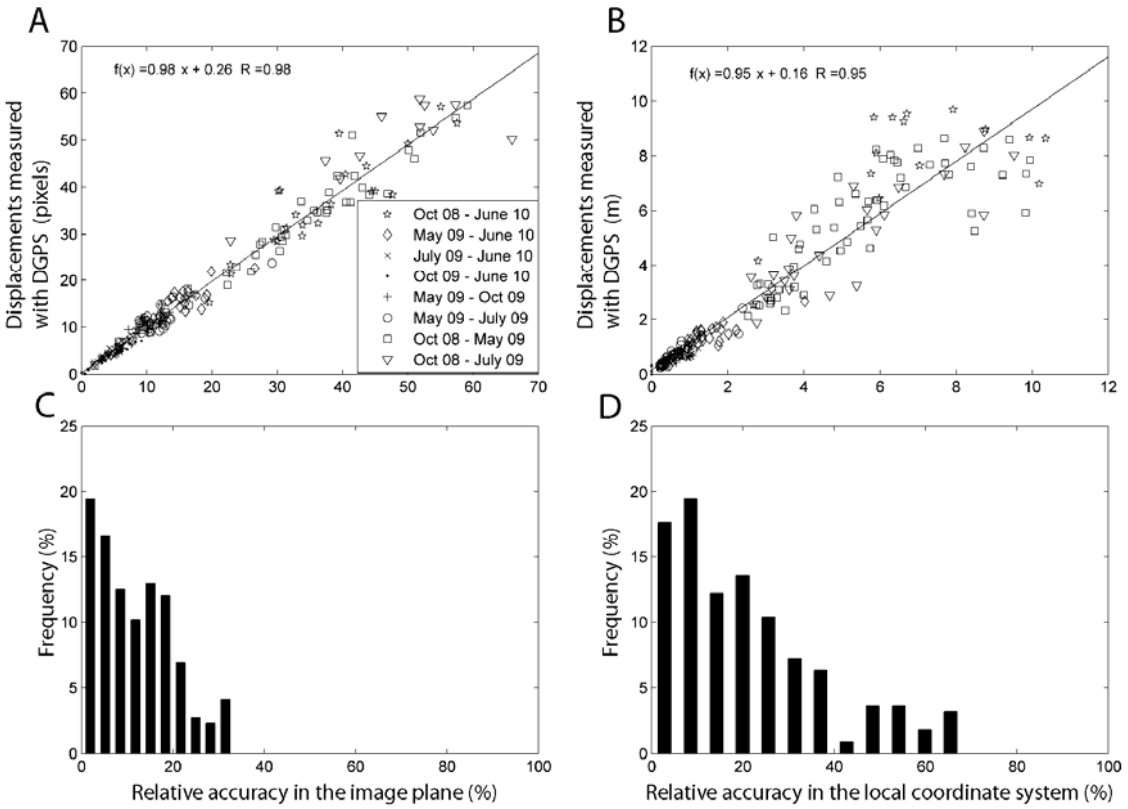


Fig. 11. Assessment of the accuracy of the Image Correlation technique. Relationships between the displacements observed by Image Correlation and the displacements observed by DGPS on sixty benchmarks in the image plane (A) and in the local coordinate system (B). Relative accuracy of the Image. Correlation technique in the images plane (C) and in the local coordinate system (D).

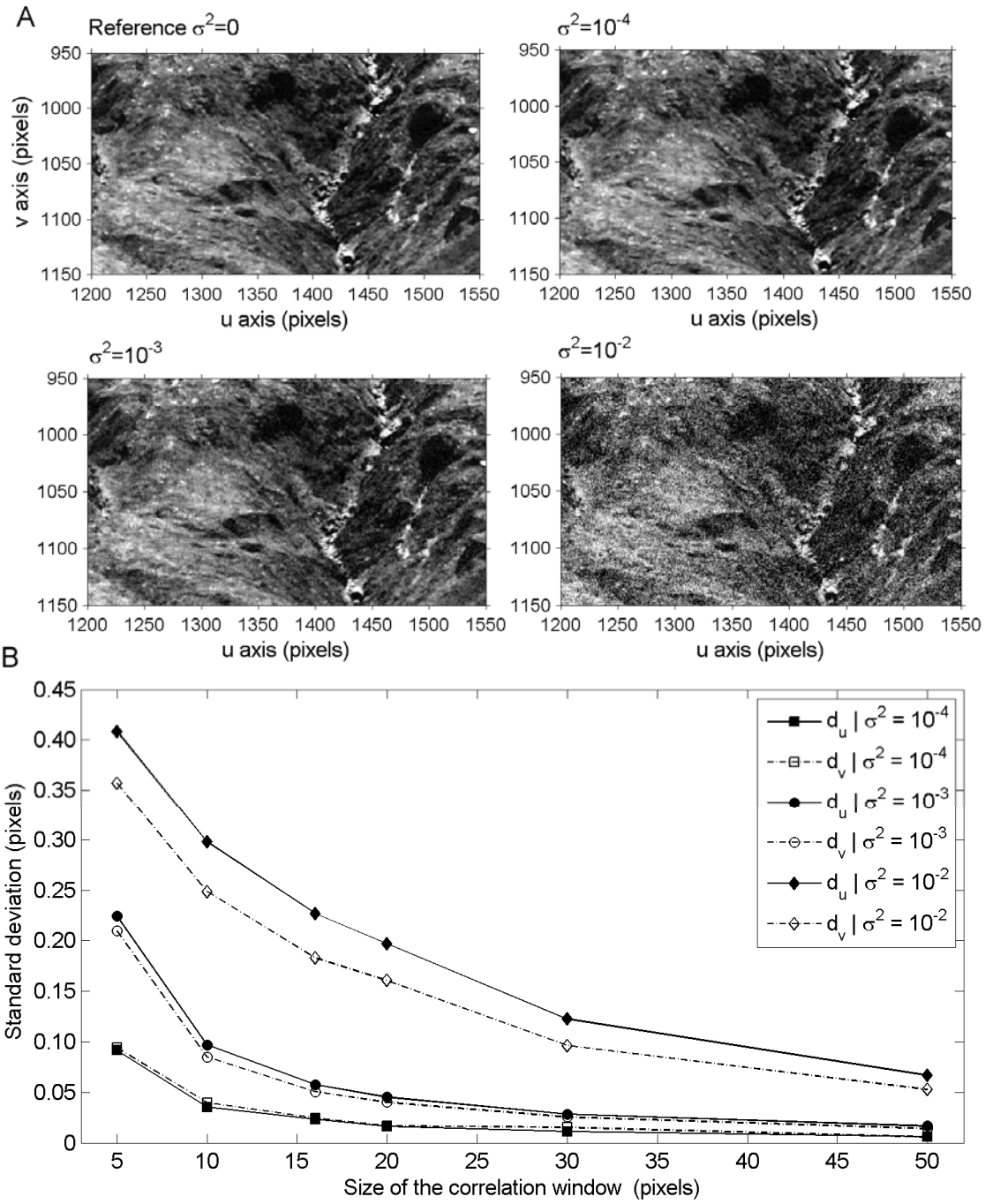


Fig. 12. Precision of the correlation algorithm. (A) Examples of different level of Gaussian noise created in the images of displacements (B) Precision of the hierarchical correlator in the *u* and *v* direction as a function of different levels of Gaussian noise (σ_n^2) and different sizes of the correlation window.

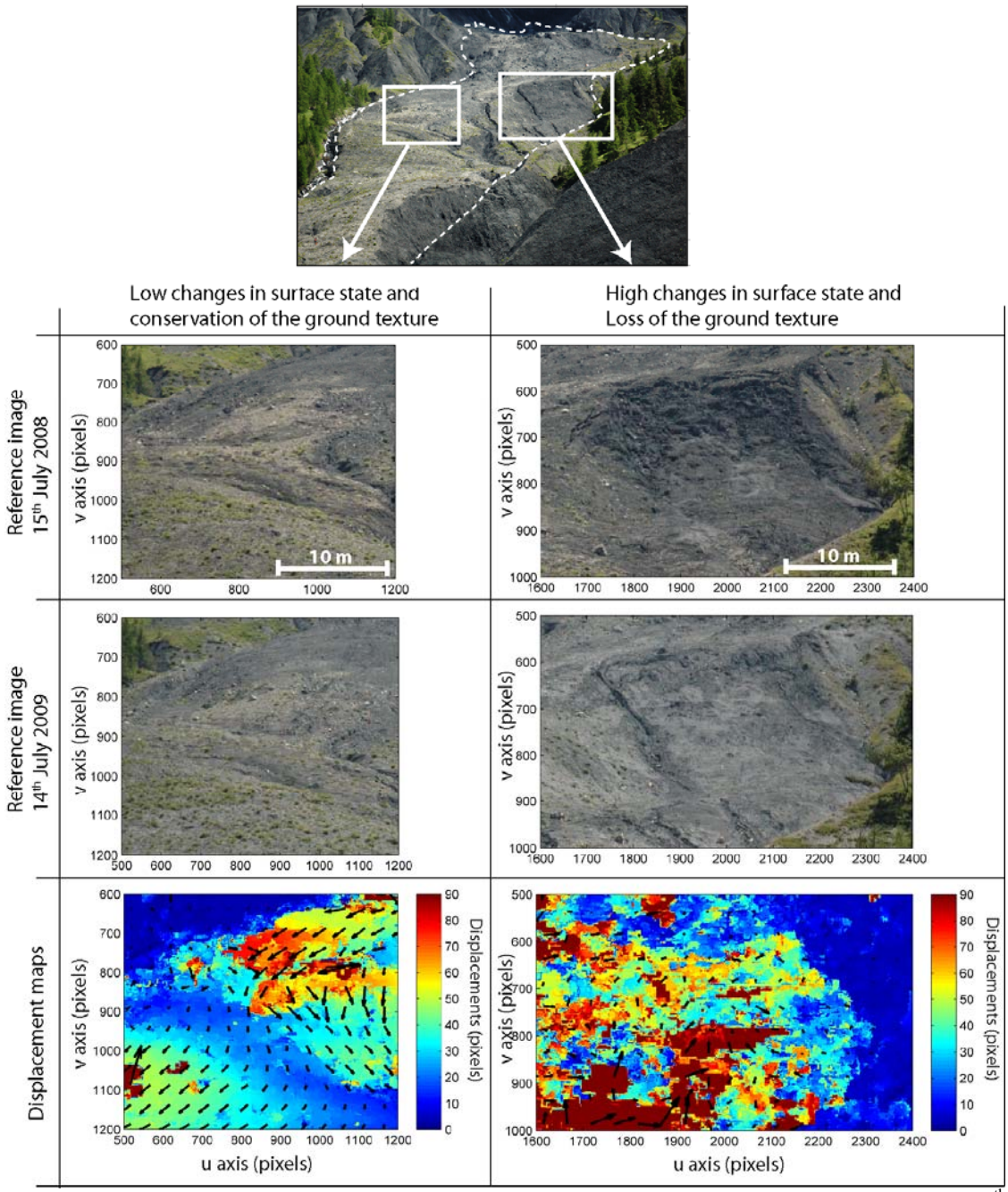


Fig. 13. Example of results for the correlation of two images acquired with one year interval (15th July 2008-14th July 2009), at the same solar time and clear sky conditions. Depending on the location in the landslide, some areas conserved their texture while others areas affected by strong weathering and ground deformation (loading of the snow and landslide displacement) display a totally different ground texture. The incoherency of the displacements is therefore clearly identifiable (inhomogeneous amplitude and direction of the displacement vectors).

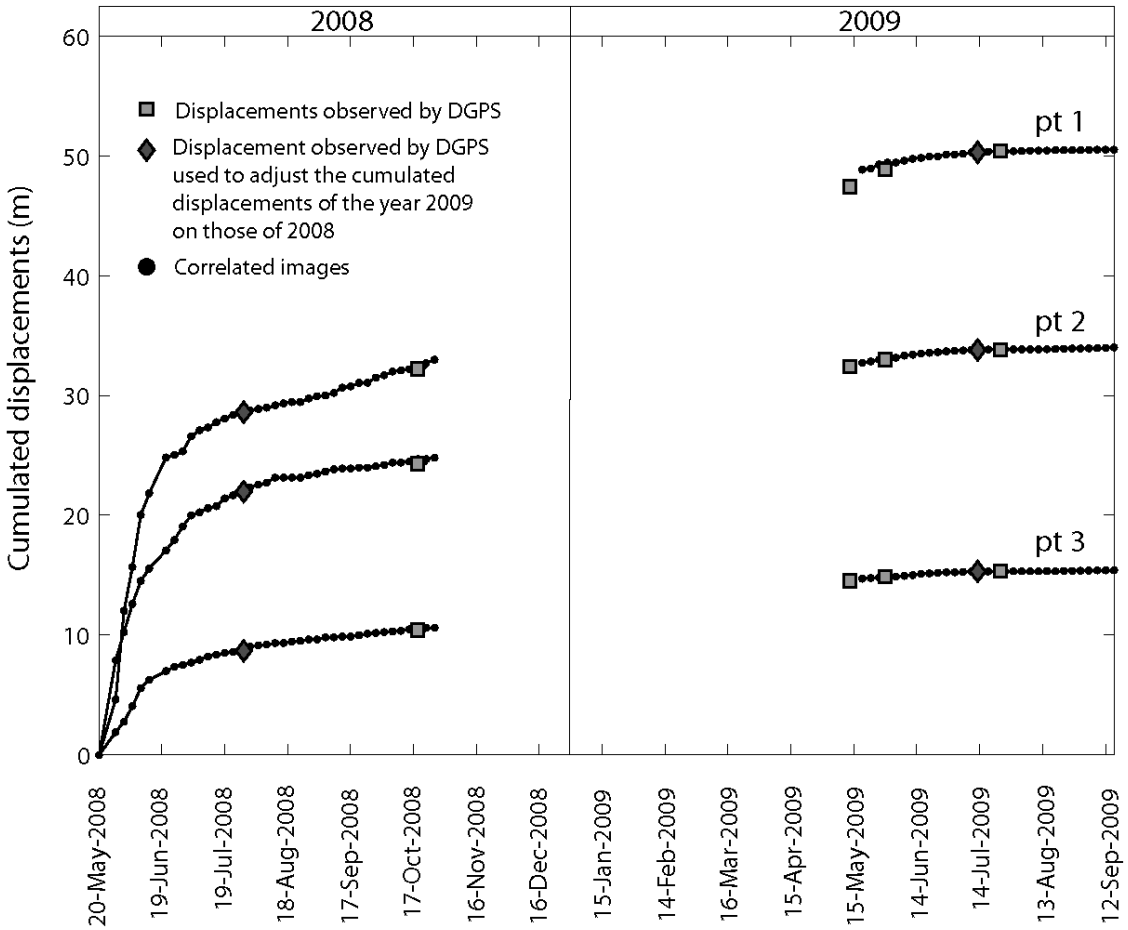


Fig. 14. Cumulated displacements at three locations in the upper (pt1), middle (pt2) and lower (pt3) parts of the landslide. The location of the points is indicated in Fig. 9. The cumulated displacements of the year 2009 are adjusted on those of 2008 using GCPs measured with DGPS at the vicinity of the points pt1, pt2 and pt3.

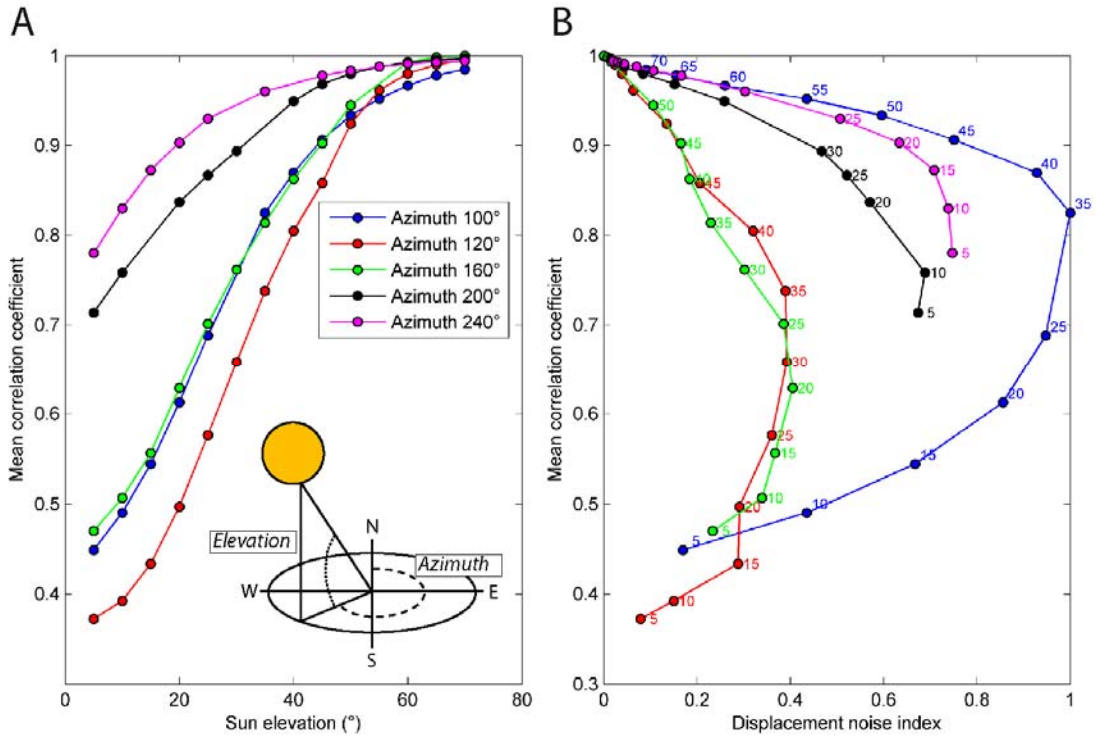


Fig. 15. Results of the correlation on the synthetic shaded relief images. (A) Influence of illumination conditions as a function of the sun elevation and azimuth on the mean correlation coefficient. (B) Relationship between displacement noise index and correlation coefficient. The values near the dots correspond to the sun elevation angles.

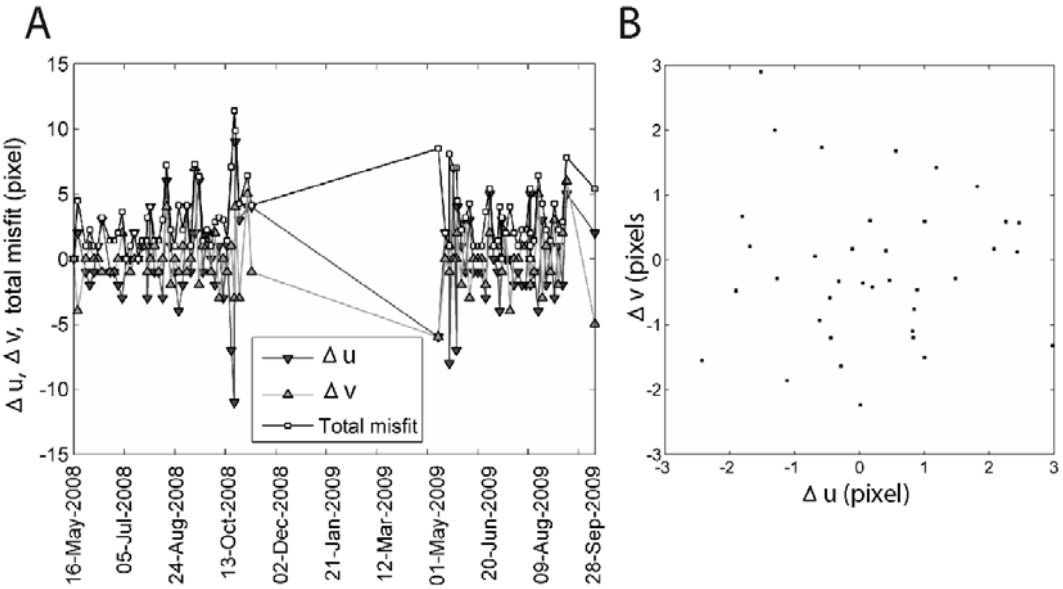


Fig. 16. Assessment of the accuracy of the camera orientation (A) Average homogenous components due to slight movement of the camera. (B) Residual Δu and Δv misfits between projected and observed GCPs after the least square minimization.

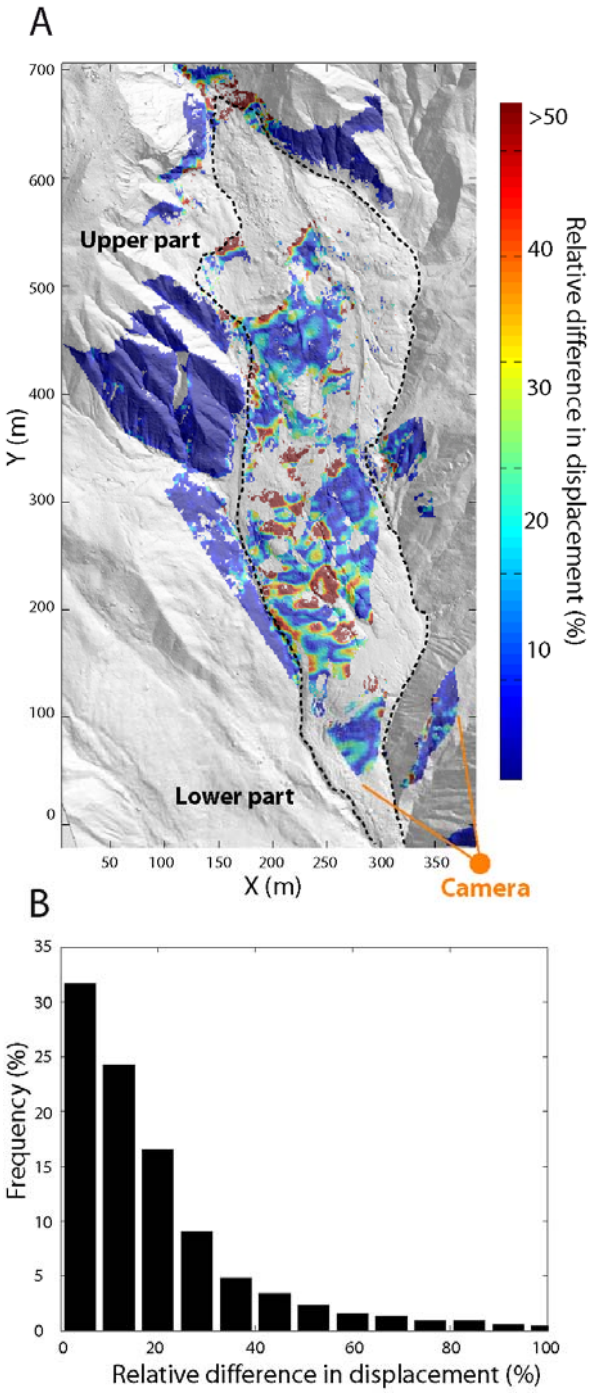


Fig. 17. Effect of the DEM on the ortho-rectification of the displacement field. (A) relative difference between the displacement field of the 1st June orthorectified with a DEM of 2007 and a DEM of 2009. (B) Histogram of the relative differences.

Tables

Table 1. Relative advantages and disadvatages for GB-InSAT, TLS and TOP

Techniques	Relative advantages	Relative disadvantages
GB-InSAR	High data accuracy possible (millimetric accuracy)	Requires large initial investment if buying
	Monitoring during night and any type of weather conditions	Skilled crew required for operation
	Atmospherics effects can be corrected (permanent scatterers)	Displacement along line of sight
	Potential for high level of automation in acquisition and post-processing	Fails in detecting large and rapid displacements (signal decorrelation)
		Sensitive to changes in acquisition geometry and surface state variations
TLS	High data accuracy possible 1-4 cm (at 100 m range); 30 cm (at 1000 m range)	Requires large initial investment if buying
	Provide an easily understandable image	Skilled crew required for operation
	Potential for high level of automation in acquisition	Computation of the true 3D displacements require specific algorithms optimized for calculations on large 3D point clouds
		Large amount of computational resources for the spatial data visualization
		Automated data post-processing difficult
TOP	High data accuracy possible from millimeters to a few centimeters at 100 m range	Adverse weather and illumination changes affects image quality
	Provide an easily understandable image	Not operating during the night
	Low initial cost and operating cost	Very Sensitive to changes in acquisition geometry and surface state variations
	Low energy supply (passive sensors)	Ortho-rectification using accurate DEM is necessary for quantitative analysis
	Potential for high level of automation in acquisition and post-processing	Ground control points necessary for camera calibration
	Simple camera calibration processes available	
	Simple matching algorithms available to produce DEMs and to compute 2D displacement fields	

Table 2. Camera acquisitions characteristics

Type of Camera	Single-lens reflex digital camera
Effective Pixels	6.1 million
Image Sensor	RGB CCD, 23.7 x 15.6 mm
Image Size	3008 x 2000
Sensitivity	400 iso
Focal length	52 mm
Shutter speed	1/800
Storage Media	CompactFlash™ (CF) Card
Storage System	NEF (RAW)

Table 3. Quantity of interpretable displacement values in summer and in autumn after filtering according to the location in the landslide (Fig. 2)

	Total		1. Correlation coefficient > 0.6		2. Downslope displacements		3. Displacements in visible areas	
23 July - 27 July 2008	Absolute quantity of values (-)	Relative quantity of values (%)	Absolute quantity of values (-)	Relative quantity of values (%)	Absolute quantity of values (-)	Relative quantity of values (%)	Absolute quantity of values (-)	Relative quantity of values (%)
Upper part	210637	100	197139	93.6	164275	78.0	161221	76.5
Middle part	24821	100	23612	95.1	23266	93.7	22343	90.0
Lower part	61979	100	61255	98.8	59989	96.8	57801	93.3
Whole landslide	297437	100	282006	94.8	247530	83.2	241365	81.1
19 Oct. - 23 Oct. 2008								
Upper part	210637	100	183570	87.2	82149	39.0	74798	35.5
Middle part	24821	100	22847	92.1	20751	83.6	18672	75.2
Lower part	61979	100	61762	99.7	60019	96.8	57510	92.8
Whole landslide	297437	100	268179	90.2	162919	60.4	150980	50.8

Table 4. Mean μ and standard deviation σ of the absolute accuracy for the projection in the image plane and the back-projection in the local coordinate system

Image plane (n=40)	μ (pixels)	σ (pixels)
u	0.20	1.59
v	-0.08	1.51
Local coordinate system (n=11)	μ (m)	σ (m)
X	0.07	0.41
Y	-0.13	0.53
Z	0.01	0.29